Uranian satellite formation from a circumplanetary disk generated by a giant impact

Yuya ISHIZAWA

A thesis submitted for the degree of Doctor of Philosophy

in the

Department of Astronomy
Kyoto University

February 12, 2021

Abstract

Uranus has a large axial tilt $\sim 90^\circ$ and its regular satellites are orbiting almost on the equatorial plane of Uranus and have nearly circular orbits. As one of the most favorable candidate for the origin of these satellites, there is a giant impact scenario. A giant impact is a collision between proto-planets in the early stage of the formation of the Solar system. A giant impact scenario is the process that ejected materials around the planet through a giant impact is accumulated by self-gravity and eventually become satellites. This scenario is possible to explain the both origin of the large axial tilt and the regular satellites of Uranus. A giant impact is usually investigated by using the smoothed hydrodynamics (SPH) method. The impact simulations for Uranus were performed so far and they shows that a giant impact could explain the large axial tilt of Uranus. They also found that sufficient amount of materials to form the Uranian satellites could be ejected around Uranus. However, whether the Uranian satellites can actually form from such a circumplanetary disk remains unclear.

Here, we investigated the process of the satellite formation from a disk generated by a giant impact, using gravitational N-body simulation, which describes accumulation of solid particles under self-gravity, in order to explain the mass-orbit distribution of the current satellites of Uranus. we developed N-body simulation code for satellite formation, including gravitational interaction, collision, and merger between particles.

In Chapter 2 (Ishizawa et al., 2019), we modeled a debris disk of solids with several initial conditions inferred from the hydrodynamic simulations and performed N-body simulations to investigate in-situ satellite formation from the debris disk. We found that, in any case, the orbital distribution of the five major satellites could not be reproduced from the disk as long as the power index of its surface density is less than $\sim$2, which is similar value to that of the disk generated just after the giant impact. The satellites in the middle region obtained much larger masses than Ariel or Umbriel, while the outermost satellites did not grow to the mass of Oberon. Our results indicate that it is necessary to consider the thermal and viscous evolution of the evaporated disk after the giant impact to form the five major satellites through giant impact scenario.

In Chapter 3 (Ida et al., 2020), we show, by means of a theoretical model, that the Uranian satellite formation is regulated by the evolution of the impact-generated disk. We predict that the disk lost a substantial amount of water vapor mass and spread to the levels of the current system until the disk cooled down enough for ice condensation and accretion of icy particles to begin. From the predicted distribution of condensed ices, we found that the circumplanetary disk of solid ice could finally have a positive gradient in radial direction. We performed the N-body simulation for it and found that it is able to reproduce the observed mass-orbit configuration of the Uranian satellites.

Acknowledgements

First of all, I would like to express my great appreciation to my supervisor, Dr. T. Sasaki. He invited me to the field of astrophysics and planetary science, and supported my research activities. Suggestions and comments from him was very insightful and essential. I'm grateful to Dr. N. Hosono for his suggestions and comments to developing numerical codes. I also thank Prof. S. Ida and S. Ueta for important discussions. Finally, I am deeply grateful to Prof. S. Mineshige for his important advises and supports.

The N-body simulation in this study was conducted at the Yukawa Institute Computer Facility. This work was supported by JSPS KAKENHI grant number 19K03950, 20J15020.

Contents

List of Figures

List of Tables

Chapter 1

Introduction

1.1 The Uranian system

1.1.1 Uranus

Uranus is the seventh planet in the Solar System and orbits at roughly 19 AU from the Sun. Physical characteristics of Uranus are listed in Table 1.1. The Uranian

TABLE 1.1: Physical characteristics of Uranus

Mass	$M_{\rm U}$	8.68×10^{25}	kg
Equatorial Radius	$R_{\rm U}$	2.56×10^{7}	m
Mean density	$\rho_{\rm U}$	1.27	g/cm^3
Rotation period	$T_{\rm U}$	6.21×10^{4}	s
Axial tilt		97.77°	

mass, $M_{\rm U}$, is 8.68×10^{25}kg and it is roughly 14.5 times of Earth. As seen in Table 1.1, the axial tilt of Uranus is about 98 degrees and it is very large with compared to other plants in the Solar System. For example, that of Neptune is about 23 degrees. The origin of the its large axial tilt is not known with certainly, but one of general speculations is that during the formation of the Solar System an Earth-sized protplanet collided with Uranus and the rotation axis is tilted (Safronov, 1966).

1.1.2 Satellites

Uranus has twenty seven satellites, which are divided into three groups: thirteen inner satellites, five major satellites and irregular satellites. Physical and orbital properties of the five major satellites are listed in Table 1.2. The five major satellites account for more than 99% of the total mass of satellites $M_{\rm tot}$, where $M_{\rm tot} \simeq 1.05 \times 10^{-4} M_{\rm U}$.

TABLE 1.2: Physical and orbital properties of the five major satellites

Satellites	m ($M_{\rm U}$)	ρ (g/cm^3)	a ($R_{\rm U}$)	i (degrees)	e
Miranda	7.59×10^{-7}	1.20	5.088	4.34	0.0013
Ariel	1.56×10^{-5}	1.59	7.481	0.04	0.0012
Umbriel	1.35×10^{-5}	1.46	10.41	0.13	0.0039
Titania	4.06×10^{-5}	1.66	17.05	0.08	0.0011
Oberon	3.47×10^{-5}	1.56	22.79	0.07	0.0014

Note: Parameters m, ρ, a, i and e stand for mass, mean density, semi-major axis, orbital inclination and eccentricity of a satellite

Thirteen inner satellites and five major satellites are called regular satellites. The regular satellites of Uranus have entirely small orbital inclinations (≤ 0.5) except for Miranda and small eccentricities (≤ 0.01). Uranus has also rings with negligible inclinations (≤ 0.1). These features means that the regular satellites and rings are placed almost on the equatorial plane of Uranus. The Uranian system, except for the irregular satellites, is tilting as a whole.

Figure 1.1 shows the mass distribution of the regular satellites. As seen in Fig. 1.1, the five major satellites orbit in the region from $5R_{\rm U}$ to $23R_{\rm U}$ in order of Miranda, Ariel, Umbriel, Titania and Oberon from the inner side and the inner satellites orbit in the inside that of Miranda.

1.2 Formation scenarios for the Uranian satellites

How these satellites are formed? Several scenarios have been proposed so far to explain the origins of satellites including the Uranian satellites.

- Gas-starved disk model (e.g., Canup & Ward, 2002, 2006): Satellite growth and loss are repeated in the circumplanetary disk produced by a slow inflow of gas and ice-rock solids from solar orbit during the end stages of the formation of the Solar System. When the mass supplies terminate, the last generation of this cycle are left in orbits.

- Viscous spreading disk model (e.g, Crida & Charnoz, 2012): A disk of solid material around a planet, like Saturnian rings, spread due to the disk's viscosity beyond the Roche limit (inside which planetary tides prevent aggregation).

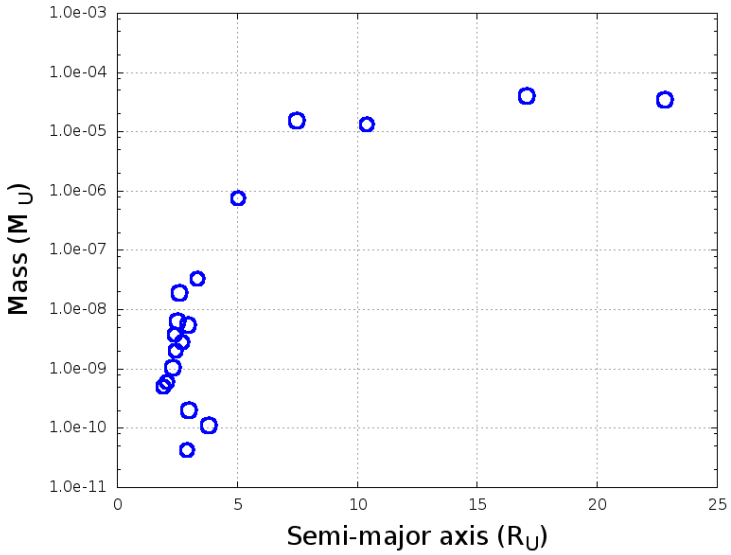

FIGURE 1.1: The mass distribution of the regular satellites orbiting around Uranus. The horizontal axis indicates the semi-major axes of the satellites normalized by the Roche limit and the vertical axis indicates the satellite mass normalized by the Uranian mass with log scale. The satellites are represented as circles. Satellites in the region from $5R_{\rm U}$ to $23R_{\rm U}$ are the five major satellites: Miranda, Ariel, Umbriel, Titania and Oberon in this order from the inner side.

Satellites are formed outside the Roche limit, migrate outward due to the tidal torque from the planet and the disk.

- Giant impact scenario (e.g, Slattery et al., 1992; Kegerreis et al., 2018): A planetary body collide with a planet, materials from the two bodies are ejected around. The ejected materials form a disk around the planet and one or more satellites are formed from the disk.

The representative studies of these scenarios are presented bellow in more detail.

Gas-starved disk model

During the final stages of the planet's formation, a giant planet has a circumplanetary disk formed by its gravitational contraction and inflow of gas to the planet become slowly as the circum-solar gas nebula begins to dissipate. Gas in the disk diffuses viscously and spreads both inward onto the planet and outward to the outer edge of the disk. Small solids are also delivered with gas from solar orbit to the disk. Satellites grow by the aggregation of solids in the disk and evolve their orbits by interaction the gravitational interaction with gas in the disk.

Canup & Ward (2006) considered a model in which satellites grow within an actively supplied circumplanetary disk, sustained by a time-dependent inflow of gas and solids from solar orbit during the end stages of the planetary formation. Such disk is called "gas-starved disk". They assumed in the model that the amount of

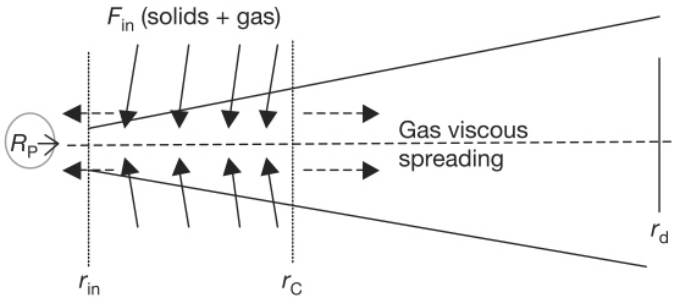

FIGURE 1.2: A schematic image of a circumplanetary disk with gas inflow and a gas spreading, viewed edge-on (Canup & Ward, 2006). Gas and solids from solar orbit flow into the disk in the region from an inner radius r_{in} to an outer radius r_C (represented as solids arrow). Gas spreads inward onto the planet and outward to the edge of the disk r_d (represented as dashed arrow).

gas in the disk is under a quasi-steady state by a balance between the inflow supply and the spread of gas since a gas spreading time is shorter than the typical time over which the gas inflow changes as the dissipation of the circum-solar gas nebula. As a satellite grow in the disk, the satellite receives a net negative torque resulting from the gravitational interaction with gas in the disk and its orbital radius decays through so-called type I migration (e.g., Ward, 1986). A satellite grow until it falls onto the planet, so the maximum satellite mass is determined by a balance between the timescale over which the satellite grows and timescale of its orbital decay. They simulated the satellite growth and loss in the disk which is sustained by a time-dependent inflow of gas and solids. As a result, they suggest that a ratio of the total satellite mass to the host planet's mass is regulated to $\sim 10^{-4}$ commonly and it depends quite weakly on both a gas-to-solids mass ratio in the inflow and a parameter characterizing the strength of viscous turbulence in a gas disk. This model can explain the composition of the satellites, especially the Galilean satellites of Jupiter, and it is favored as the formation of Galilean satellites.

The satellite system mass fraction of Uranus is also roughly $\sim 10^{-4}$. They suggest also that the Uranian satellites' properties are consistent with those produced in their

model but the large axial tilt of Uranus requires additional explanation.

Viscous spreading disk model

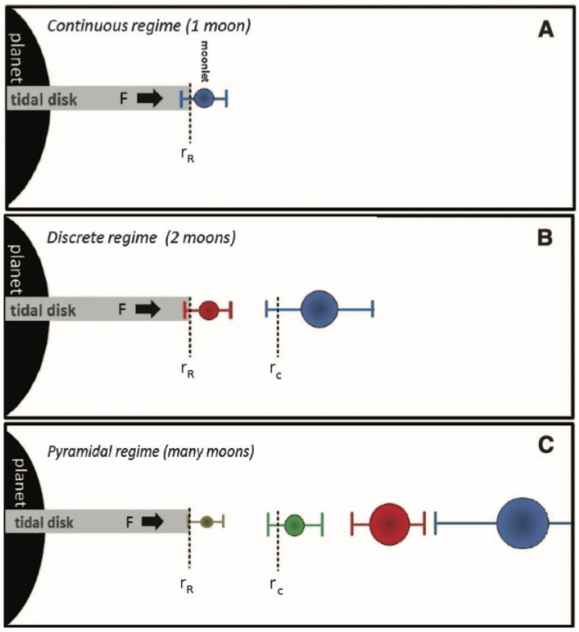

FIGURE 1.3: A schematic process of formation and orbital evolution of satellites from the tidal disk, viewed edge-on (Crida & Charnoz, 2012). In their model satellite accretion proceeds in three regimes. F indicates the mass flow at the edge of the tidal disk. (**A**) Continuous regime: The first satellite (represented in blue) is formed from materials which spread beyond the Roche limit r_{R}. The first satellite migrate outward with getting mass from the disk. (**B**) Discrete regime: When the first satellite reaches a certain critical radius r_{c}, it can not immediately accrete materials from the disk anymore. Then, a new satellite is formed (represented in red), migrate faster than the first one and accreted to the first one e before the new one reaches r_{c}. (**C**) Pyramidal regime: When the first satellite leaves far away enough, the second satellite is formed independently and other moons are formed in the same way. In this regime mergers also occur between satellites side by side with similar masses. Finally after these regimes of formation and orbital evolution, mass distribution of satellites become pyramidal.

Crida & Charnoz (2012) consider an analytic model for the accretion and orbital evolution of satellites from a disk of solid materials around a planet. The inner edge of the disk is the planet's radius and the outer edge is the Roche limit, inside which the tidal force of the planet prevents aggregation. Such a tidal disk spread due to the disk's viscosity (Daisaka et al., 2001) beyond the Roche limit and then a satellite is formed by the disk's mass flow outside the Roche limit. In their model, the satellite

formed outside the Roche limit migrate outward by receiving negative tidal torque from the planet and the disk. In the same way a new satellite is formed outside the edge of the disk and migrate. When a satellite is formed the disk mass decreases and the disk's mass flow also decrease, so the formed satellite mass gradually become small with generation. The migration speed of a satellite decreases with its orbital radius and an inner satellite can reach the region in which an outer satellite can merge with it. When the differences between masses and orbital radii of satellites side by side become large enough, the mergers between them do not occur since the migration speed decreases also with the planet's mass and the timescale of the satellite accretion become large as the disk mass decreases. Figure 1.3 shows a schematic process of these satellite growth.

They analytically investigated the accretion and migration of satellites in several parameters. As a result, they suggest that the mass distribution with orbital radii of regular satellites of Saturn, Uranus, and Neptune can be explained by their model. In their model it is assumed that formed satellites do not perturb each other ' s orbit or the disk. They assumed also significantly strong tidal dissipation inside Saturn as the tidal quality factor $Q_{\rm p} = 1680$ and applied this value to the other planet's condition (see Section 2.3).

Hyodo et al. (2015) performed direct numerical simulations of the satellite formation in the such disks as modeled by Crida & Charnoz (2012) to investigate the more realistic dynamical effect on the accretion and orbital evolution of satellites. They confirmed that one or two satellites are formed from the disks at least. The origin of a tidal disk is not explicit but they suggest that a tidal disk can be produced by tidal disruption of a passing comet in heliocentric or a satellite to fall inside the Roche limit.

Giant impact scenario

A giant impact is a high energetic collision between protoplanets during the end stages of formation of the Solar System protoplanets. In a giant impact scenario, one or more satellites are formed from a circumplanetary disk generated by a large planetary body's impact to an early planet. Figure 1.4 shows a schematic process of the satellite formation on the basis of a giant impact scenario. A giant impact scenario includes following three steps.

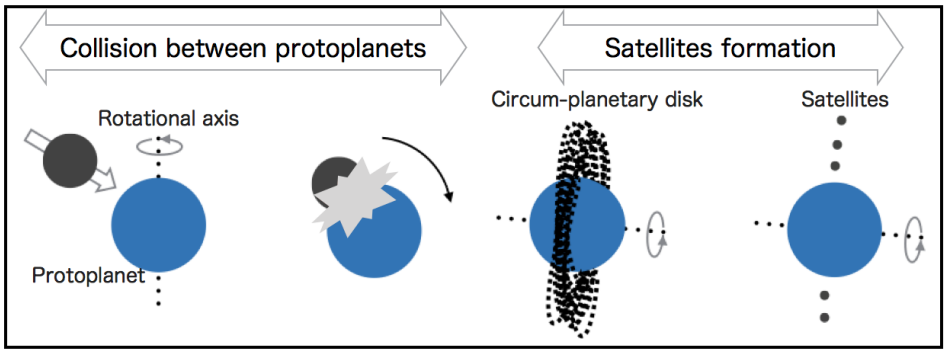

FIGURE 1.4: A schematic process of a giant impact scenario. First, two protoplanets collide with each other and then materials of the two bodies ejected around. Second, satellites are formed from a circum-planetary disk of ejected materials.

1. Collision between protoplanets

2. Evolution of a circumplanetary disk

3. Satellite formation

A giant impact is a high energetic collision and it is usually modeled by using the smoothed-particle hydrodynamics (SPH) method, in which the fluid elements are represented by particles. Slattery et al. (1992) performed hydrodynamic simulations of collisions between a model of primitive Uranus and impactors with masses ranging from one Earth's mass to three Earth's masses (Figure 1.5). In their simulations, total angular momentum in the system is varied as a parameter. They conclude that a fairly large range of giant impacts that could have produced the rotational period and the large axial tilt of Uranus in the present. They also suggest that Uranian regular satellites could be formed accreting materials ejected in orbit.

The disk produced by a giant impact has high energy and high temperature just after the impact considered to experience some cooling process. However, it is difficult to simulate the disk evolution by the SPH method since the SPH method has difficulties in dealing with hydrodynamical instabilities. Ward (2017) analytically investigated evolution of a circumplanetary disk formed by a giant impact. He examined evolutions of two-phase disks in vapor/melt and water/steam equilibrium in the cases for a terrestrial planet (e.g., Earth) and an ice giant planet (e.g., Uranus), respectively. He modeled hypothetically a water/steam disk placed within the Roche limit around an ice giant planet in which viscous heating dominates. He suggest that

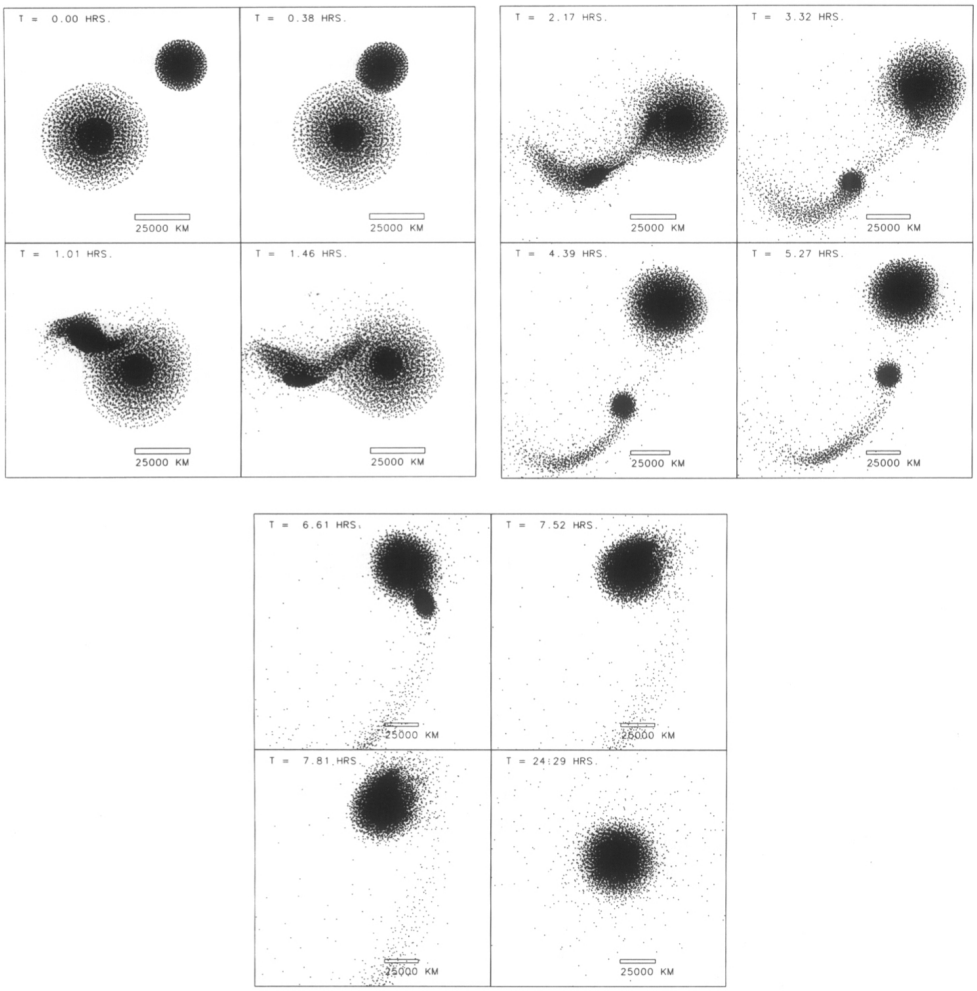

FIGURE 1.5: Snapshots of one of the results for simulations of giant impact performed by Slattery et al. (1992) using the SPH method.

in such hypothetical disk there could be the regions partially and totally vaporized. However, it is still uncertain how a circumplanetary disk generated by a giant impact experiences evolves through radiative cooling, some dynamical effects and chemical reactions.

The satellite accretion after a giant impact in the case of Uranus is not well investigated numerically but in the case of the Earth-moon system have been investigated (e.g., Ida et al., 1997; Kokubo et al., 2000). It is commonly considered that a circum-Earth's disk produced by a giant impact has several times of lunar mass and placed within several times of the Earth radius. On the other hand, Uranus has the multi-satellite system placed within almost twenty five times of the Uranian radius, so it may be difficult to consider the satellite accretion from such narrow disk compared to the current satellite system.

1.3 Purpose and composition of this thesis

1.3.1 Toward Uranian satellite formation

There are, as above, several models to explain the origin of the Uranian satellites but there is not the leading model so far. These models, except for giant impact scenario, needs additional explanation for the large axial tilt of Uranus to satellite formation. On the other hand, in giant impact scenario, the detail of the impact-generated disk had been not known well until recently because of limits of calculation performance of SPH method, which needs high computational costs. In the simulations by Slattery et al. (1992) the number of particles which describe Uranus and a impactor is 8,000, so the mass of one particle exceeds the sum of masses of the current satellite system.

Kegerreis et al. (2018); Reinhardt et al. (2020) performed the SPH simulations describing giant impacts into Uranus with high resolution compared to Slattery et al. (1992). Kegerreis et al. (2018) suggest that giants impact into Uranus could form the disk which reaches a few tens of the Uranian radius, which includes the current orbits of the regular satellites of Uranus. They also suggest that the a giant impact of an Earth-sized protoplanet with proto-Uranus could tilt the rotational axis, and a circumplanetary disk would be generated throughout the current Uranian satellites orbits by the impact, although materials of the disk are highly concentrated. It is may be possible to form the current satellites of Uranus around the each current site.

1.3.2 Purpose and composition

Here, in this thesis, we adopted a giant impact scenario as a possible process to form the Uranian regular satellites. We investigated the process of the satellite formation from a disk generated by a giant impact, using gravitational N-body simulation, which describes accumulation of solid particles under self-gravity, in order to explain the mass-orbit distribution of the current satellites of Uranus.

In Chapter 2 (Ishizawa et al., 2019), we modeled a debris disk of solids with several initial conditions as inferred from the hydrodynamic simulations and performed N-body simulations to investigate in-situ satellite formation from the debris disk.

In Chapter 3 (Ida et al., 2020), we show, by means of a theoretical model, that the Uranian satellite formation is regulated by the evolution of the impact-generated

disk. We analytically predicted the distribution of condensed ices and performed the N-body simulation for it to investigate whether it can explain the mass-orbit configuration of the Uranian satellites or not.

Chapter 2

Satellite formation from a debris disk

2.1 Calculation method

We considered a model in which satellites grow within a wide circumplanetary disk of solids and performed N-body simulations to investigate the in-situ formation of Uranian regular satellites. An N-body simulation describes a dynamical system of particles, mainly under gravity. Here, a particle represents a small rock-ice solid body that eventually forms a satellite. The calculations consider gravitational interaction, collision, and merger between particles. In the following N-body simulation, mass, distance, and time are respectively normalized by the Uranian mass $M_{\rm U}$, Roche limit $a_{\rm R}$ given by

$$a_{\rm R} = 2.456 \left(\frac{\rho}{\rho_{\rm U}} \right)^{-\frac{1}{3}} R_{\rm U} = 2.38 R_{\rm U}, \tag{2.1}$$

and inverse of angular velocity at Roche limit $\Omega_{\rm R}^{-1}$ given by

$$\Omega_{\rm R} = \sqrt{\frac{GM_{\rm U}}{a_{\rm R}^3}}, \tag{2.2}$$

where G is the gravitational constant; $\rho = 1.40$ g cm^{-3}, the mean density of the satellite system; $\rho_{\rm U} = 1.27$ g cm^{-3}, the density of Uranus; and $R_{\rm U} = 0.42 a_{\rm R}$, the Uranian radius. Inside the Roche limit, the planet's tidal force exceeds the relatively small body's self-gravity. Therefore, a satellite cannot accrete inside the Roche limit; however, it can do so outside this limit.

2.1.1 Numerical method

Particle orbits are calculated according to the following equation of motion.

$$\frac{d^2\boldsymbol{r_i}}{dt^2} = -GM_{\rm U}\frac{\boldsymbol{r}_i}{|\boldsymbol{r}_i|^3} - \sum_{i\neq j} Gm_j \frac{\boldsymbol{r}_j - \boldsymbol{r}_i}{|\boldsymbol{r}_j - \boldsymbol{r}_i|^3}, \tag{2.3}$$

where $\boldsymbol{r_i}$ and m_i are respectively the position relative to the center of Uranus and mass of particle i. We used a fourth-order Hermite scheme (Makino & Aarseth, 1992) for time integration during the growth of inner particles, and also used the second-order Leap Frog method during the growth of outer particles. We adopted a shared time-step and changed it from $2^{-9}\Omega_{\rm R}^{-1}$ to $2^{-5}\Omega_{\rm R}^{-1}$ depending on particle growth.

Because the computational cost of calculating the gravitational interaction between all particles is expensive, we adopted the Framework for Developing Particle Simulator (FDPS), a library for particle-based numerical simulations, developed by Iwasawa et al. (2016). FDPS provides functions for efficient parallelization of calculations and reduces the calculation cost of the interaction from $\mathcal{O}(N^2)$ to $\mathcal{O}(N\log N)$, where N is the total number of particles introduced to the system..

The simulations consider interparticle collisions. Specifically, such a collision is detected when the distance between two particles becomes smaller than or equal to the sum of their radii. Collisions are assumed to be moderately inelastic. The relative velocity of two colliding particles changes according to the following equation:

$$\boldsymbol{v}_{\boldsymbol{n}}' = -\epsilon_n \boldsymbol{v_n} \tag{2.4}$$

$$\boldsymbol{v}_{\boldsymbol{t}}' = \epsilon_t \boldsymbol{v_t} \tag{2.5}$$

where $\boldsymbol{v}'$ and $\boldsymbol{v}$ are respectively the relative velocity after and before a collision and the subscripts n and t respectively represent normal and tangential components. We set the normal component of the coefficient of restitution ϵ_n to 0.1 and the tangential component ϵ_t to 1, and we neglect particle spin for simplicity. The velocities of two particles after a collision are determined based on the law of conservation of momentum. Two particles must be separated as the distance between their centers equals the sum of their radii to avoid an unnecessary collision in the next time step; this separation is carried out under the law of conservation of angular momentum (see Appendix A.1).

If the relative velocity of two particles after a collision is smaller than the surface escape velocity modified by the tidal force, they are gravitationally bounded. In rotational coordinates around Uranus at distance a with Kepler angular velocity Ω, such conditions are described by negative Jacobi energy $E_{\rm J}$ of the two particles after the collision:

$$E_{\rm J} = \frac{1}{2}|v|^2 - \frac{3}{2}x^2\Omega^2 + \frac{1}{2}z^2\Omega^2 - \frac{G(m_1+m_2)}{r} + \frac{9}{2}r_{\rm H}^2\Omega^2 < 0, \tag{2.6}$$

where m_1 and m_2 are the masses of the two particles; x, y, and z are the relative positions of the two particles; r is the distance between the two particles, and $r_{\rm H}$ is the Hill radius defined by

$$r_{\rm H} = \left(\frac{m_1+m_2}{3M_{\rm U}}\right)^{\frac{1}{3}} a, \tag{2.7}$$

which is the region dominated by the attraction of the two particles. The Jacobi energy can be negative even when the center of masses of the two particles is outside the Hill sphere. For the two particles to be gravitationally bounded, the following condition must also hold:

$$r_1 + r_2 \leq r_{\rm H}, \tag{2.8}$$

where r_1 and r_2 are the radii of the two particles. The two particles are gravitationally bounded when both conditions Eqs.(2.6) and (2.8) are satisfied (Kokubo et al., 2000).

In the following N-body simulations, gravitationally bound particles are merged into one spherical particle. The merging of the two particles is calculated based on the laws of conservation of total mass and momentum. Collisional fragmentation of particles is not considered here because an increase in the number of particles greatly increases the calculation costs.

2.1.2 Initial conditions of debris disks

Just after a giant impact occurs, vaporized materials and the atmosphere of Uranus and the impactor are ejected, resulting in the presence of high-temperature gas disk as well as rock solids. The gas disk formed from the ejected materials around Uranus

evolves through dynamical processes, chemical reactions, and radiative cooling. Then the disk gas density would significantly decay due to the viscous diffusion before the ice condensation to form the debris disk. We have investigated disk evolution after a giant impact to Uranus in detail in Chapter 3(Ida et al., 2020).

In this study, we focus on satellite accretion from debris disks of solids in a gas-free environment. To investigate the types of debris disks suitable for in-situ formation of Uranian satellites, we simulated the evolution of debris disks with several initial conditions. We considered the total mass and surface density distribution of debris disks as the most important factors in the satellite formation process.

We set the initial disk mass ($M_{\rm disk}$) to be several times the total mass of the current Uranian satellite system ($M_{\rm tot} \sim 10^{-4} M_{\rm U}$). The surface density distribution is assumed to follow a power law with semi-major axis a and is represented as $\Sigma(a) \propto a^{-q}$. q is set as 3.00, 2.15, 1.95, and 1.50 as inferred from the density profiles in the results by Kegerreis et al. (2018). Table 2.1 shows the model sets of the initial disks with the masses and power-indexes of the surface density distribution.

TABLE 2.1: Model set of initial conditions

Model	$M_{\rm disk}[M_{\rm tot}]$	q
Disk1	3	1.50
Disk2	4	2.15
Disk3	10	2.15
Disk4	4	1.95
Disk5	3	1.95
Disk6	3	3.00

The inner edge of the disk is Uranian radius. Although the outer edge of the disk is not shown explicitly in Kegerreis et al. (2018), we set the outer edge to be $25 a_{\rm U}$ which includes the orbit of the outermost satellite, Oberon, by simply extrapolating from the results of Kegerreis et al. (2018). We assumed that the initial eccentricities and inclinations of disk particles follow a Rayleigh distribution. The root-mean-square of the eccentricity $\langle e^2 \rangle^{\frac{1}{2}}$ is set to be 0.3 and that of the inclination $\langle i^2 \rangle^{\frac{1}{2}}$ is set to be 0.15. The other orbital elements of disk particles are set randomly. The number of disk particles is 10,000 in all models. The density of disk particles is $\rho = 1.40$ g cm^{-3} as inferred from the density of the Uranian satellite system. Disk particles are assumed

to be rigid spheres. The physical radius of a disk particle is given by

$$r_{\rm p} = \left(\frac{m}{M_{\rm U}}\right)^{\frac{1}{3}} \left(\frac{\rho}{\rho_{\rm U}}\right)^{-\frac{1}{3}} R_{\rm U} = \frac{1}{2.456} \left(\frac{m}{M_{\rm U}}\right)^{\frac{1}{3}} a_{\rm R}, \tag{2.9}$$

where m is the particle mass. The initial masses of particles are equal to each other.

2.2 Results

We performed N-body simulations of satellite formation for the six disk models. The mass is normalized by $M_{\rm tot} \sim 10^{-4} M_{\rm U}$ and time is normalized by $T_{\rm K}$, which is the Kepler period at the distance of the Roche limit and is given by

$$T_{\rm K} = \frac{2\pi}{\Omega_{\rm R}} \approx 10.9 \text{ hour}. \tag{2.10}$$

2.2.1 Mass distributions with semi-major axis

Figure 2.1 shows the particle accumulation result for Disk1 [$M_{\rm disk} = 3M_{\rm tot}$, $q = 1.50$], which is the mass distribution of grown-up particles and the outer four satellites (Ariel, Umbriel, Titania, and Oberon) differentiated by time from $t = 6.4 \times 10^4 T_{\rm K}$ to $2.5 \times 10^6 T_{\rm K}$. The isolation mass distribution for the initial disk is also shown in each panel (see Appendix A.2). In the inner region of the disk, the local surface density and velocity dispersion of particles are larger than those in the outer region, and gravitational encounters between particles occur more often. Therefore, the particle growth timescale increases as the distance from Uranus increases.

The grown-up particles at $t = 2.5 \times 10^6 T_{\rm K} (\sim 3100$ years) have comparable masses to each other, and their particle masses range from $0.1 M_{\rm tot}$ to $0.4 M_{\rm tot}$. With compared to the current satellites, the grown-up particles in the inner region have much larger mass than the inner thirteen moons($< 10^{-7} M_{\rm tot}$), and in the middle region ($3R_{\rm U}$ to $13R_{\rm U}$), several particles with a few times mass of Ariel or Umbriel are formed. On the other hand, the two outermost grown-up particles have less masses and less orbital radii than the two outermost satellites, Titania and Oberon, respectively. The total mass of the grown-up particles is around $1.9 M_{\rm tot}$; this is around 64% of the initial disk mass. The mass that falls into Uranus from the disk is around $0.85 M_{\rm tot}$; this is around 28 % of the initial disk mass.

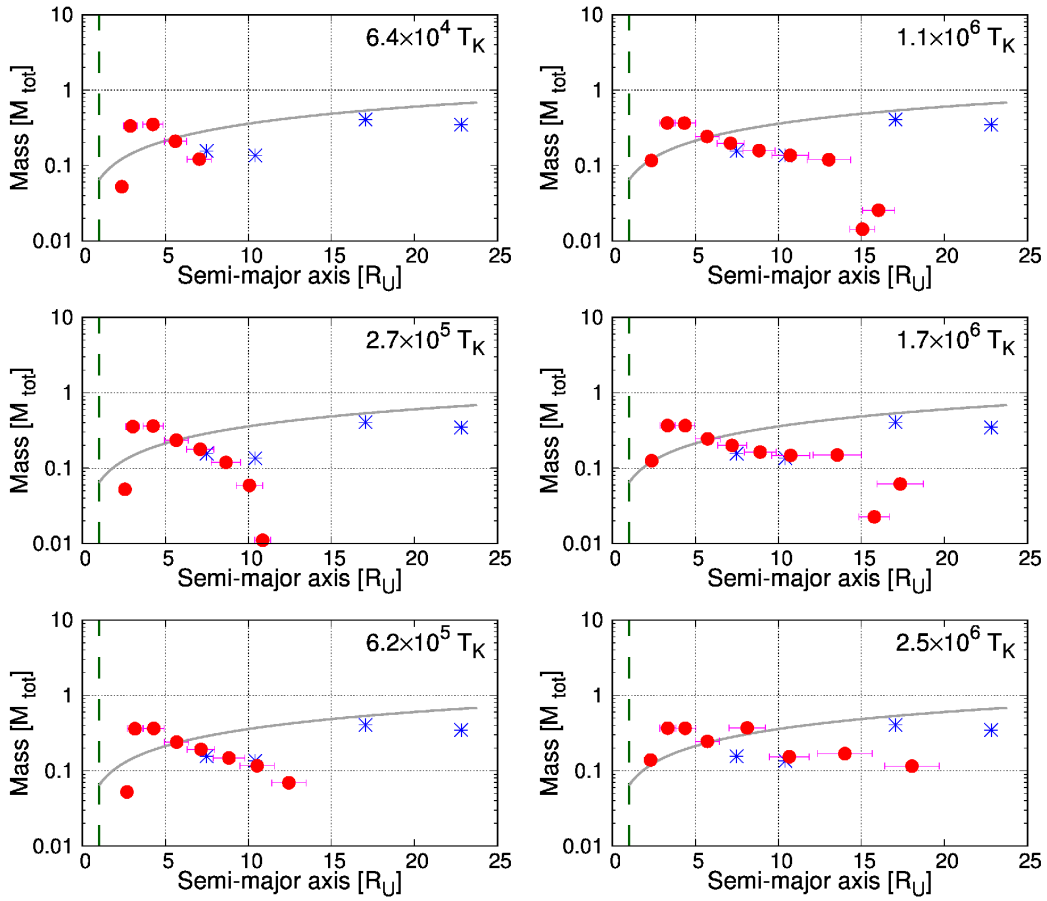

FIGURE 2.1: Time series of satellite mass distribution for Disk1 [$M_{\rm disk} = 3M_{\rm tot}, q = 1.50$]. The red filled circles represent grown-up particles in this simulation, and the lines from their centers to both sides have length of $5r_{\rm H}$. The blue stars represent Ariel, Umbriel, Titania, and Oberon in the current satellite system. The dashed lines indicate the Uranian radius and the solid lines indicate the isolation mass distribution for the initial disk. $2.5{\times}10^6 T_{\rm K}$ equals $\sim$ 3100 years.

Similar results are obtained for Disk2 [$M_{\rm disk} = 4M_{\rm tot}$, $q = 2.15$], shown in Fig. 2.2, differentiated by time from $t = 1.6 \times 10^5 T_{\rm K}$ to $5.9 \times 10^6 T_{\rm K}$. Disk2 has slightly larger mass and larger value of q than Disk1. Particles grow with timescales similar to those for Disk1. The particle distribution is similar to that of Disk1; inner extra particles, more particles with higher masses in the middle, and two outermost particles with less masses and less orbital radii. The total mass of the grown-up particles is around $2.4M_{\rm tot}$; this is around 61% of the initial disk mass. The mass that falls from the disk into Uranus is around $1.4M_{\rm tot}$; this is around 35 % of the initial disk mass.

Figs. 2.3-2.6 shows the results for Disk3 at $t = 7.4 \times 10^5 T_{\rm K}$, for Disk4 at $t = 5.7 \times 10^6 T_{\rm K}$, for Disk5 at $t = 5.7 \times 10^6 T_{\rm K}$, and for Disk6 at $t = 5.4 \times 10^5 T_{\rm K}$. Fig. 2.3 shows that the total mass of the grown-up particles for Disk3 is $6.8M_{\rm tot}$; this is too

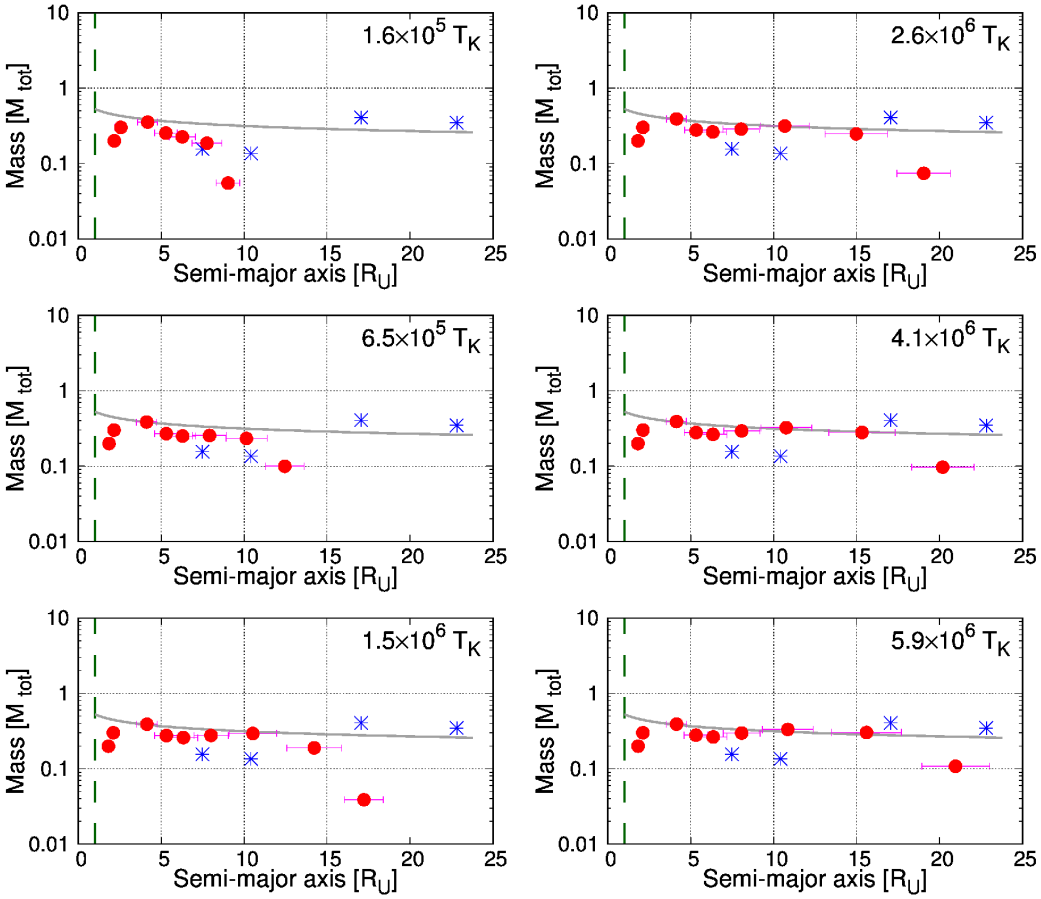

FIGURE 2.2: Same as Fig. 2.1 but for Disk2 [$M_{\rm disk} = 4M_{\rm tot}$, $q = 2.15$].

much compared with that of the current satellites. Fig. 2.4 (Disk4) and Fig. 2.5 (Disk5) show that the initial conditions are similar but distributions are slightly different because of the stochastic effect during particle growth. In these results, the particle with comparable mass and orbit to Umbriel's formed, and the outermost particle has similar orbit of Oberon but still much less mass. The sums of grown-up particles' mass in the outer region are $1.5M_{\rm tot}$ for Disk4 and $1.1M_{\rm tot}$ for Disk5. Fig. 2.6 (Disk6) shows that the mass of grown-up particles decreases sharply with the semi-major axis and that the mass distribution obviously differs from that of the current satellites.

Summarizing the results from the above-described disk models, the particle distribution from any above-described disk models could not directly reproduce the satellite distribution. However, the orbital evolution of particles with long timescale after their growth can alter the mass-orbit distribution. of the grown-up particles, so we take it into account in Section 2.3.

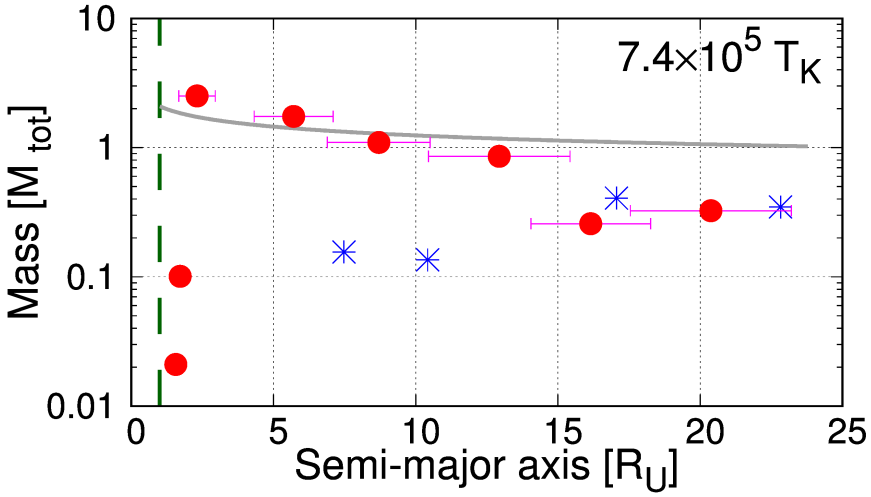

FIGURE 2.3: Disk3 [$M_{\rm disk} = 10M_{\rm tot}$, $q = 2.15$]

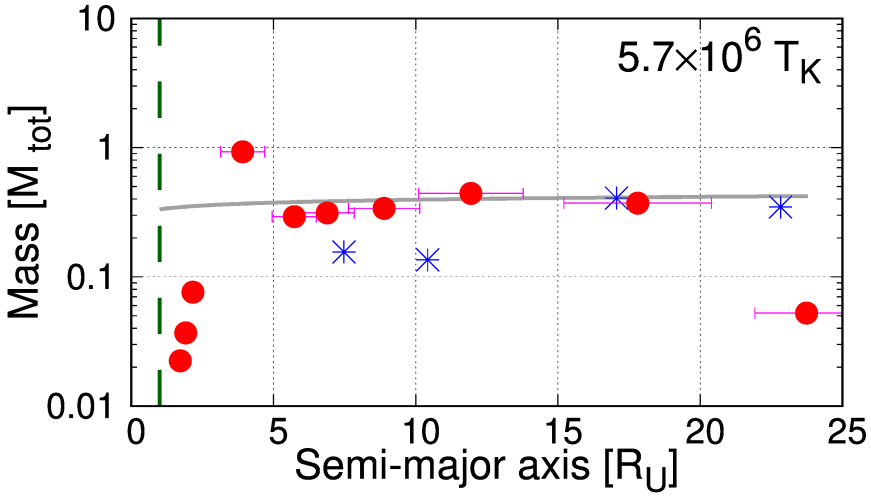

FIGURE 2.4: Disk4 [$M_{\rm disk} = 4M_{\rm tot}$, $q = 1.95$]

We note that particle growth in the above-described disk models has not been completed. Disk particles accounting for some percentage of the initial disk mass remain in each disk. Such particles can accrete to grown-up particles; alternatively, they can be cleared away from the system because of scattering with other particles in the later stage and can damp the eccentricities and inclinations of grown-up particles. However, they do not largely change the orbital radius and mass of grown-up particles. Even if all remnant particles in orbits accrete to the outermost particle, in the all results here except for Disk3, its mass can not reach the mass of Oberon.

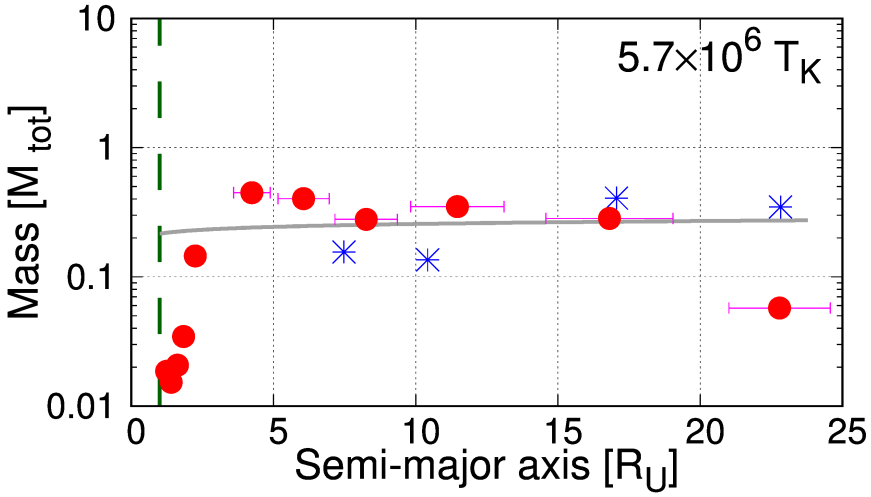

FIGURE 2.5: Disk5 [$M_{\rm disk} = 3M_{\rm tot}$, $q = 1.95$]

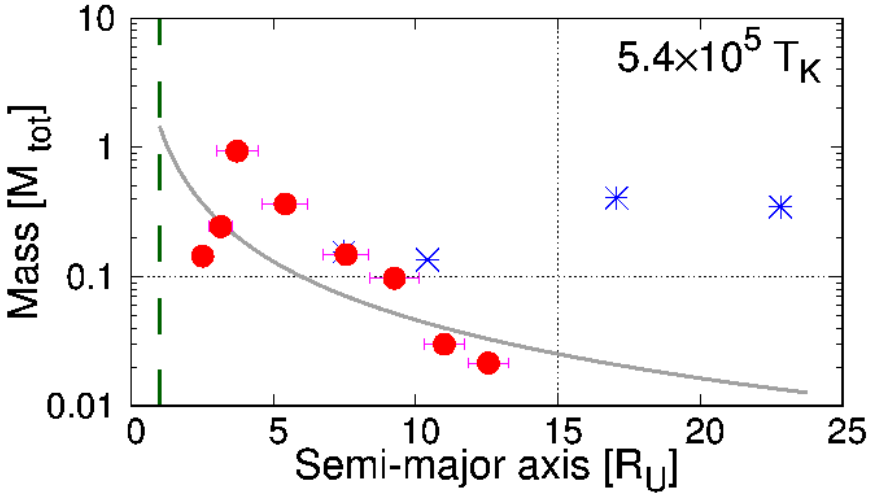

FIGURE 2.6: Disk6 [$M_{\rm disk} = 3M_{\rm tot}$, $q = 3.00$]

2.2.2 Comparison with isolation mass

When the power index q is much larger than 2, as in the case of Disk6, the mass distribution shows a sharply decreasing slope with the semi-major axis and becomes greatly different from that of the current satellite system. Even if the effects of radial diffusion, orbital evolution, and some stochastic fluctuations are considered, the condition $q \geq 3$ is not suitable for in-situ formation of the current satellite system.

When the power index q is around 2, as in the cases of Disk2, Disk3, Disk4, and Disk5, the mass distribution of the grown-up particles becomes almost flat. For example, for Disk2 (Fig.2.2), particles grow with the isolation mass distribution; however, there is a small difference owing to the effect of radial diffusion and stochastic

fluctuation. The distributions for Disk4 and Disk5, especially in the inner regions, differ from each other despite the same power index because of the stochastic effect. The stochastic effect can arise largely from gravitational interactions in the packed orbits of the inner grown-up particles in the early stage; this is analogous to the giant impact regime in planetary formation.

When the power index q is less than 2, as in the case of Disk1 (Fig.2.1), the isolation mass is predicted to increase with the semi-major axis. However, the distribution of the isolation mass, especially in the inner region, greatly differs from that of grown-up particles. This may mainly be caused by mass transfer from the outer orbits due to radial diffusion.

By using curve fitting analogous to least squares approximation, the isolation mass function (Eq.A.11) can be fitted to the data distribution of the masses and the orbital radii of the outer four satellites. Then, q and $M_{\rm disk}/M_{\rm tot}$ are fitted to be 1.36 and 1.76, respectively; these are close to the parameters for Disk1. Even if $q < 2$ including the fitted value for the outer four satellites, several extra satellites with larger masses than the isolation mass distribution could form in the inner region unless q is a very low or negative value.

2.3 Discussion

2.3.1 Orbital evolution after satellite growth

The particle distribution from the above-described disk models could not reproduce the mass-orbit distribution of the current satellites, but it can be affected by orbital evolution of particles after their growth. Since the timescale of the orbital evolution is much larger than that of the satellite growth, which is less than thousands years, the main orbital evolutions would occur after the satellite growth. Orbital evolution of a satellite mainly occurs owing to gas drag in satellite orbits, tidal torque from a central planet, tidal dissipation in the interior of the satellite, and gravitational interaction with other satellites.

Our calculations do not consider the existence of gas. Gas infall from the interplanetary region can be considered a possible cause of the existence of gas in the circum-Uranus region. However, in the giant impact regime of the formation of

the Solar system, gas may have dissipated from the Uranian orbit (e.g., Lissauer & Stewart, 1993).

A tidal torque is caused by a difference between the rotational period of Uranus and the orbital period of a satellite. Angular momentum is transferred between the planet and the satellite, and therefore, the satellite orbit evolves. The orbital radius of a satellite whose orbital period corresponds to the rotational period of Uranus $T_{\rm U}$ is called the corotation radius $r_{\rm c}$, and it is expressed as

$$r_{\rm c} = \left(\frac{T_{\rm U}}{2\pi}\right)^{\frac{2}{3}} (GM_{\rm U})^{\frac{1}{3}}. \tag{2.11}$$

At present, $T_{\rm U}$ =17h 14m 24s = 62064s; then, $r_{\rm c}$ = 3.30 $R_{\rm U}$. The corotation radius normalized by the Roche limit is $r_{\rm c}$ = 1.39 $a_{\rm R}$ for ρ = 1.40. A satellite inside the corotation radius receives negative torque from Uranus and migrates inward, whereas one outside the corotation radius receives positive torque and migrates outward.

Tidal dissipation occurs in the interior of a satellite with an eccentric orbit owing to the tidal force generated by a planet; it can act to heat the satellite and damp its eccentricity. The tidal torque depends on the composition of Uranus, and tidal dissipation mainly depends on the composition of the satellite.

The semi-major axis a and the eccentricity e of a satellite evolve according to the following equations (Charnoz et al., 2010):

$$\frac{{\rm d}a}{{\rm d}t} = {\rm sgn}(a - r_{\rm c}) \frac{3k_{2\rm p} M G^{1/2} R_{\rm p}^5}{Q_{\rm p} M_{\rm p}^{1/2} a^{11/2}} \left(1 + \frac{51e^2}{4}\right) - \frac{21 k_2 n M_{\rm p} R^5}{QMa^4} e^2, \tag{2.12}$$

$$\frac{{\rm d}e}{{\rm d}t} = {\rm sgn}(a - r_{\rm c}) \frac{57 k_{2\rm p} n M R_{\rm p}^5}{8 Q_{\rm p} M_{\rm p} a^5} e - \frac{21 k_2 n M_{\rm p} R^5}{2QMa^5} e, \tag{2.13}$$

where $k_{2\rm p}$ (k_2), $Q_{\rm p}$ (Q), $M_{\rm p}$ (M), and $R_{\rm p}$ (R) are the tidal Love number, tidal quality factor, mass of the planet, and radius of the planet (satellite), respectively, and n is the satellite's orbital frequency. The first term in each equation accounts for tidal torque from Uranus and the second term accounts for tidal dissipation in the interior of the satellite. For a satellite orbiting inside (outside) the corotation radius, the first term becomes negative (positive). These evolution rates largely depend on the satellites' semi-major axes.

We analytically calculated the orbital evolution of grown-up particles over 4.5 billion years for Disk1 and Disk2 according to Eqs.(2.12) and (2.13); the results are

shown in Fig.2.7. We set the tidal Love number of Uranus as $k_{2\mathrm{p}} = 0.104$ (Gavrilov & Zharkov, 1977); tidal quality factor of Uranus as $Q_{\mathrm{p}} = 11,000$, which is the lower limit of the constrained value by Tittemore & Wisdom (1989); and tidal parameters of the particles as $k_2/Q = 10^{-5}$ with reference to Tittemore & Wisdom (1989). In these analytic calculations, the gravitational interaction between particles is not considered and the corotation radius is assumed to be the same as the present one during orbital evolution.

As shown in Fig.2.7, particles inside the corotation radius fall to the planet over several million years whereas particles in the region $r_{\mathrm{c}} \leq a \lesssim 10R_{\mathrm{U}}$ move outward and merge each other in several billion years. By contrast, particles in the region $a \gtrsim 10R_{\mathrm{U}}$ would mostly remain in their orbits over billions of years. This is because the evolution rate of a particle's orbit is affected largely by its semi-major axis rather than by its mass. According to the orbital evolution of satellites owing to tides, inner extra particles around the corotation radius would move out of this region. However, the particles in the middle region would increase its mass to several times after migration and merger, so it would eventually obtain further mass compared to Ariel or Titania. On the other hand, the outermost satellites would not change their orbits and masses.

Inside the corotation radius, the particles which migrate inward would be disrupted by Uranus' tidal force, and their fragments would form a ring inside the Roche limit. The inner small satellites can form from such rings based on the model proposed by Crida & Charnoz (2012). According to this model, in order to form these inner small satellites, the mass of the satellite-forming ring would need $\sim 1.06 \times 10^{-3} M_{\mathrm{tot}}$.

Hesselbrock & Minton (2019) suggested that, under the ring-satellite system, Miranda could have formed and evolved out only to about 4 Uranian radii, and not to 5 Uranian radii where it is now (as ring torques cannot act beyond the 2:1 outer resonance with ring edge at the Roche limit). So Miranda may have originally formed close to 5 Uranian radii where it is now.

Conclusively we suggest that, even if the effect of the orbital evolution is taken into account, the orbital distribution of the five major satellites could not be reproduced from the above-described disk, where the power index of its surface density is similar to that of the disk generated just after the giant impact. In order to explain that outer two satellites (Titania and Oberon) exceed the two middle satellites (Ariel and

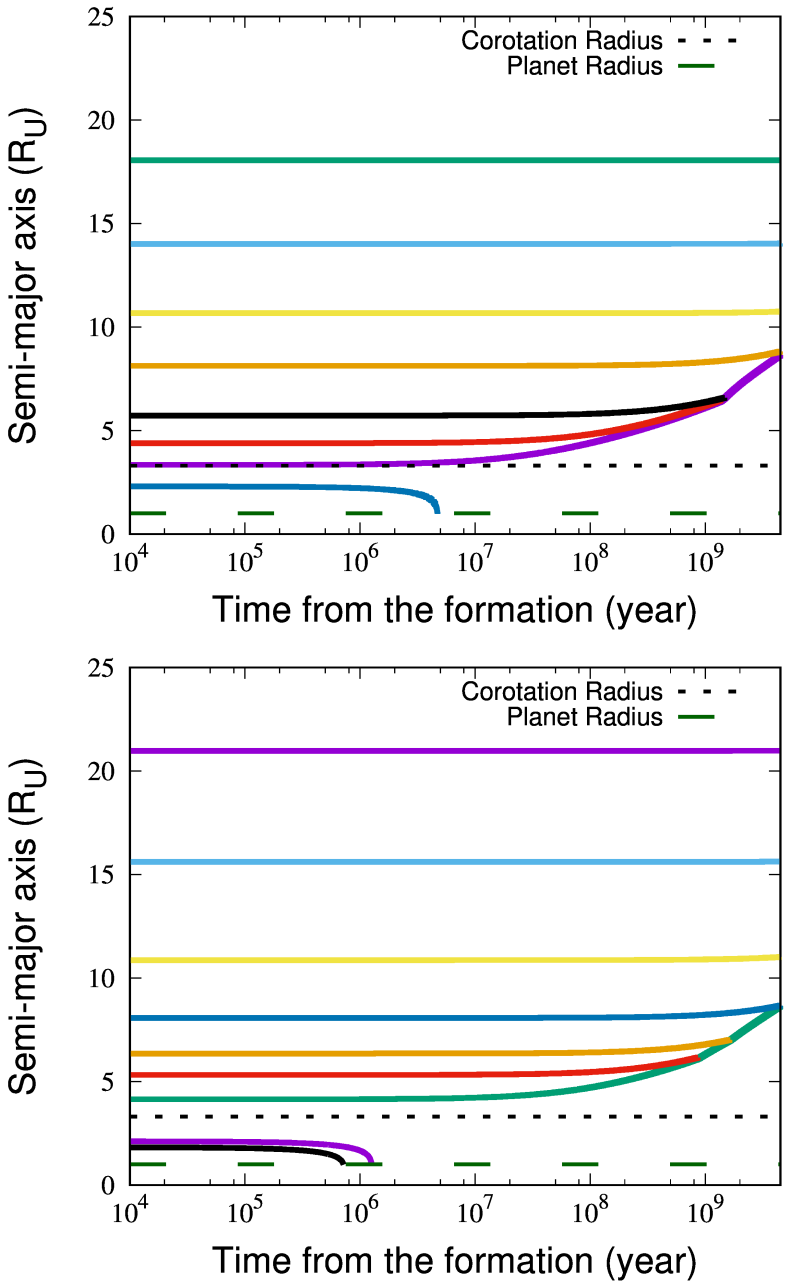

FIGURE 2.7: Tidal evolution of orbits of grown-up particles for Disk1 (upper panel) and Disk2 (lower panel). Solid lines indicate orbital evolution of particles with time, and long and short dashed lines respectively indicate the Uranian radius and corotation radius. Here, gravitational interaction between particles is not considered. When particles' orbits overlap, they are merged into one based on the law of mass conservation.

Umbriel) in their masses through in-situ formation, the initial debris disk should have a mass distribution of solids that increases with distance from Uranus, which seems counter-intuitive for material distribution inferred from giant impact simulations. We speculate that a evaporated disk after a giant impact would experience some thermal and viscous evolution, and then the five massive satellites would form from a disk of solids whose q value is much less than 1.5 or negative (namely, the power index of its surface density is positive), whose outer edge reach around the orbit of Oberon. Even in such a situation, orbital migration of satellites inside the corotation radius can occur, so if a satellite inside the corotation radius have $10^{-3}M_{\rm tot}$ at least, it can migrate into the Roche limit within 4.5 billion years, and then the small inner satellites are still possible to form from rings generated by the disruption of it.

2.4 Conclusion

We modeled a wide debris disk generated by the giant impact, performed N-body simulations of satellites accretion in such a disk, and investigated the possibility of the in-situ formation of the Uranian satellites, taking account of the orbital evolution of satellites due to the planetary tides after their growth. We found that, from such disks, satellites in the middle region ($3R_{\rm U}$ to $13R_{\rm U}$) would have much larger masses than Ariel or Umbriel, and the outermost satellite would not obtain a mass of Oberon, so the orbital distribution of the five major satellites could not be reproduced.

However, we still believe that the five major satellites would form in the current site since it would be difficult to form from rings inside the Roche limit and migrate to the current orbits. We also notice that a evaporated disk after a giant impact should experience some thermal and viscous evolution, and then the five massive satellites would form from a disk whose q value is much less than 1.5 or negative, whose outer edge reach around the orbit of Oberon. On the other hand, the small inner satellites may form from rings generated by the satellites which moved inward and disrupted by the planetary tides (Crida & Charnoz, 2012).

It would be necessary to investigate the thermal and viscous evolution of a evaporated disk generated just after an impact into an icy giant, and then simulate the satellite formation with q be much smaller and negative to realize the possibility of the in-situ formation of the Uranian satellites based on giant impact scenario.

Chapter 3

Satellite formation via vapor disk evolution

Ishizawa et al. (2019) shows that it is difficult to reproduce the mass-orbit distribution of the current Uranian satellites from the circumplanetary disk whose mass surface density has a negative radial gradient (Chapter 2). In Ishizawa et al. (2019) it is assumed that ejected materials after a giant impact are reduced while maintaining its radial gradient.

In fact, however, as shown in the SPH simulations (Kegerreis et al., 2018), when a giant impact occurs, ejected materials including rocks are vaporized. Uranus' gravity accelerates the impact velocity to $\gtrsim 20$ km/s and then the impact energy become $\gtrsim 2 \times 10^8$J/kg, which is 100 times larger than the latent heat of water ice. The icy mantle ejected around totally vaporize and the impact-generated disk, which is formed just after a giant impact, mainly consists of water vapor and H/He gas ejected from the proto-Uranus and the impacter.

Ida et al. (2020) performed one-dimensional viscous diffusion simulations that an impact-generated disk is quickly relaxed to a quasi-steady accretion disk and also we shows that its surface density and temperature evolution are approximated by an analytical self-similar formula. We found that the ice distribution is independent of detailed structure of the initial impact-generated disk because ice condensation occurs after significant evolution of the quasi-steady disk. In the same paper, we performed a N-body simulation of the satellite formation from such disk as we derived, and found that the similar distribution to the current satellite system of Uranus could form from the predicted ice distribution.

3.1 Model

3.1.1 Viscous diffusion equation

In a gas disk rotating with centrifugal force and gravity balanced under the action of viscosity, the orbital energy of gas dissipates due to kinetic friction and is carried to local temperature of gas disk. Ida et al. (2020) treat a water vapor disk as such disk, a viscous heated disk.

As local disk temperature, they use the photo-surface temperature for simplicity, which is assumed the balance between viscous dissipation at the mid-plane of a disk and radiative cooling from its photo-surface (e.g., Lynden-Bell & Pringle, 1974; Hartmann et al., 1998),

$$T \simeq \left(\frac{9\, G M_{\rm U} \Sigma_{\rm g} \nu}{8\, \sigma r^3} \right)^{1/4}, \tag{3.1}$$

where r is the distance from Uranus, $\Sigma_{\rm g}$ is the disk surface density, and σ is the Stefan-Boltzmann constant. The turbulent kinetic viscosity is modeled by

$$\nu \sim \alpha c_s^2 \Omega^{-1}, \tag{3.2}$$

where c_s is the local sound velocity and orbital frequency of the disk gas, and α is a constant parameter to represent the turbulence strength ($\alpha \ll 1$) (Shakura & Sunyaev, 1973). c_s is described as $c_s = \sqrt{k_{\rm B} T / \mu_{\rm g} m_{\rm H}}$, where $k_{\rm B}$ is the Boltzmann constant, $\mu_{\rm g}$ is the mean molecular weight of the gas, and $m_{\rm H}$ is the hydrogen atom mass.

The viscous diffusion equation is given by (Hartmann et al., 1998)

$$\frac{\partial \Sigma_{\rm g}}{\partial t} - \frac{1}{r} \frac{\partial}{\partial r} \left[3 r^{1/2} \frac{\partial}{\partial r} (\Sigma_{\rm g} \nu r^{1/2}) \right] = 0. \tag{3.3}$$

Ida et al. (2020) numerically solve this equation with Eq. (3.1) and Eq. (3.2). The results of the evolution of the surface density and the temperature of the disk gas are shown in Fig.3.1 with solid lines. They show that the impact-generated disk quickly spreads and cools. By the conservation of total angular momentum, the spreading is associated by accretion of the disk onto the planet. The disk converges to a quasi-steady-state accretion disk where the $\Sigma_{\rm g}$ and T distributions with radial distance r evolve self-similarly. We also derive an approximate expression for the self-similar

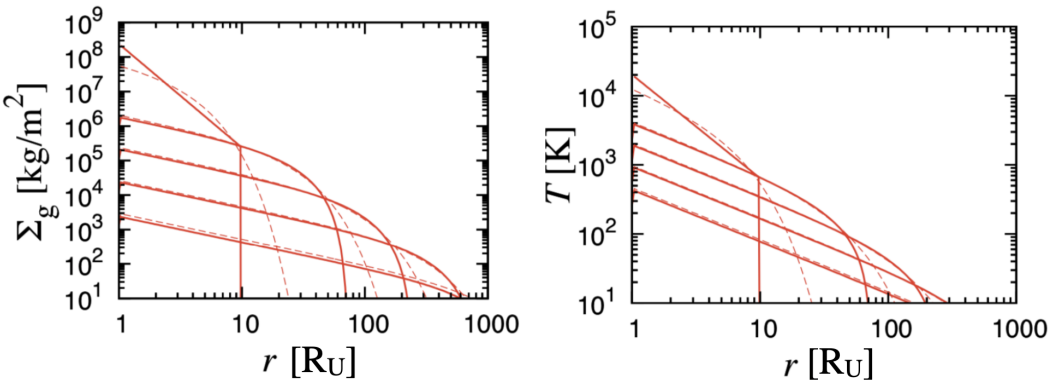

FIGURE 3.1: The evolution of the disk surface density of a mixture of H/He gas and water vapor (left panel) and the disk temperature (right panel) with $\alpha = 10^{-3}$. In these plots, the ice condensation is artificially neglected. The solid and dashed red lines are the numerically solved and analytical distributions. The analytical Σ_g is given by Eq. (B.5). The temperature is calculated by Eq. (3.1) with the obtained Σ_g. From the upper to lower curves represent the distributions at a snapshot of $t = 0, 10, 10^2, 10^3$ and 10^4 years. The initial disk for the numerical calculation is set as a centrally-confined one, with $M_{d,imp} = 10^{-2} M_U$ and $\langle r_{d,imp} \rangle \simeq 2.3\, R_U$ by setting $\Sigma_{g,imp} = 2.4 \times 10^8 (r/R_U)^{-3}\,\mathrm{kg/m^2}$ with a truncation at $r = 10\, R_U$, suggested by SPH simulations. In the analytical self-similar formula, $r_{d,0} = 3\, R_U$ and $\Sigma_{d,0} = 0.3\, \Sigma_{g,imp}$ are used, according to Eqs. (B.10) and (B.11). The numerical solution is quickly converged to the analytical self-similar solution. They agree with each other except for the low-Σ_g tail.

solution of Σ_g and T in order to generalize the numerical results (See Appendix B.1). The analytical formulae of Σ_g and T are plotted in Fig.3.1 with dashed lines and reproduce the numerical results except for the exponential tail.

3.1.2 Distribution of ice disk

When the disk temperature decays to the ice condensation temperature $T_{\rm ice} \sim 240\,{\rm K}$ (see Appendix B.2), we deposit the condensed ice surface density by $\gamma\,\Sigma_g$. SPH simulations suggest $\gamma \sim 0.1 - 0.5$ (Slattery et al., 1992; Kegerreis et al., 2018). We use $\gamma = 0.3$ as a nominal value and $\gamma_{03} = \gamma/0.3$.

With $T \simeq 240$ K, the numerically obtained $\Sigma_{\rm ice}$ and deposited radius ('ice line') $r_{\rm ice}$ are plotted in Fig. 3.2.

From Eq. (3.1),

$$T \simeq 240 \left(\frac{\alpha}{10^{-3}}\right)^{1/3} \left(\frac{\Sigma_g}{4.0\times 10^2 {\rm kg/m^2}}\right)^{1/3} \left(\frac{r}{R_{\rm U}}\right)^{-1/2} ({\rm K}). \tag{3.4}$$

Substituting $T_{\rm ice} = 240$ K for Eq. (3.4) and solving for r, we can obtain,

$$\Sigma_{\rm ice} \simeq 1.2\times 10^2 \beta^{-1}\gamma_{03} \left(\frac{r}{r_{\rm U}}\right)^{3/2} {\rm kg/m^2}, \tag{3.5}$$

where $\beta = (\alpha/10^{-3})(T_{\rm ice}/240\,{\rm K})^{-3}$. Because ice condensation occurs after substantial evolution of the quasi-steady-state disk, the ice distribution is independent of the detailed structure of the initial impact-generated disk. Here, the radial drift and diffusion of the condensed ice in the disk with time is not considered, but growth timescale is much shorter than that of radial evolution of ice particles, so we assumed that a condensed ice particle stay in the same orbit (see Section B.3). This analytical distribution completely reproduces the numerical solution of 1D diffusion equation (Fig. 3.2).

The reason why the positive gradient of $\Sigma_{\rm ice}(\propto r^{3/2})$ is produced from Σ_g with the negative slope ($\propto r^{-3/4}$) because, in inner regions, the viscous heating is more efficient (Eq. (3.1)) and the disk must be more significantly depleted to realize $T \lesssim T_{\rm ice}$ than in outer regions. The positive gradient implies that most of the condensed ice mass is located in an outermost region.

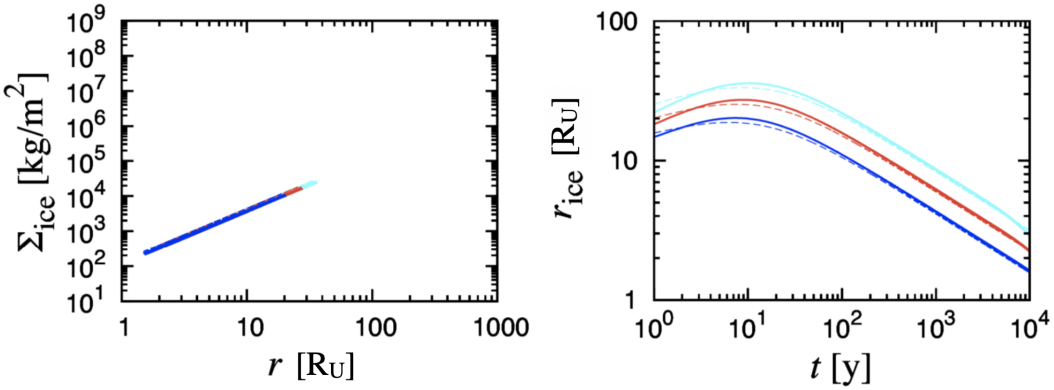

FIGURE 3.2: The distribution of the condensed ice is plotted in the left panel. The time evolution of the ice line is plotted in the right panel. The solid and dashed lines are the numerically solved distribution and the analytical distribution, respectively. The blue, red, and right blues lines are for $M_{\rm disk} = 3\times10^{-3}M_{\rm U}, 10^{-2}M_{\rm U}$, and $3\times10^{-2}M_{\rm U}$, respectively. When the disk temperature becomes equal to the ice condensation temperature, we assume that ice condenses with the surface density as $\gamma\Sigma_{\rm g}$ at that time (left panel), where we assumed $\gamma = 0.3$. The magnitude of the ice surface density is independent of the initial disk mass, while the disk mass affects how far the the distribution extends.

The ice condensation occurs when the gas temperature T become lower than $T_{\rm ice}$ for the first time at individual r. As the gas disk further expands, T in the outer regions becomes well below $T_{\rm ice}$. However, icy grains do not condense there, because the ices have already condensed and the gas there is free of water vapor. The maximum radius $r_{\rm max}$ of the ice condensation is estimated by the intersection of Eq.(3.5) and the envelope curve of the superposition of the $\Sigma_{\rm g}$-r curves at different times (Fig.3.1). It is given by (see Appendix B.1):

$$r_{\rm max} \simeq 20 \left[\beta \left(\frac{\langle r_{\rm d,imp}\rangle}{2\,R_{\rm U}}\right)^{-5/4} \left(\frac{M_{\rm d,imp}}{10^{-2}M_{\rm U}}\right)\right]^{1/4} R_{\rm U}, \tag{3.6}$$

where $M_{\rm d,imp}$ is the total mass of the impact-generated disk, $\langle r_{\rm d,imp}\rangle$ is its mean orbital radius defined by $\langle r_{\rm d,imp}\rangle = ((J_{\rm d,imp}/M_{\rm d,imp})/\Omega_{\rm U}R_{\rm U}^2)^2 R_{\rm U}$, $J_{\rm d,imp}$ is its total angular momentum, and $\Omega_{\rm U}$ is the disk orbital frequency at $r = r_{\rm U}$.

From Eqs. (3.5) and (3.6), the total condensed ice mass is

$$M_{\rm ice} \simeq \int_{r_{\rm U}}^{r_{\rm max}} 2\pi r \Sigma_{\rm ice} dr \tag{3.7}$$

$$\simeq 0.58 \times 10^{-4}\, \beta^{1/8} \gamma_{03} \left(\frac{\langle r_{\rm d,imp} \rangle}{2\, r_{\rm U}} \right)^{-5/4} \left(\frac{M_{\rm d,imp}}{10^{-2} M_{\rm U}} \right)^{7/8} M_{\rm U}, \tag{3.8}$$

which is consistent with the current total mass of Uranian satellites ($\simeq 1.0 \times 10^{-4}\, M_{\rm U}$). Although the turbulent viscosity parameter α is uncertain, the α-dependence of $M_{\rm ice}$ and $r_{\rm max}$ are very weak ($\beta \propto \alpha$). Thus, we have demonstrated that the compact ($\langle r_{\rm d,imp} \rangle \simeq 2.3\, R_{\rm U}$) and massive ($M_{\rm d,imp} \simeq 10^{-2} M_{\rm U}$) initial disk produces the condensed ice confined at a distant place, $r_{\rm max} \simeq 20 R_{\rm U}$ with the highly reduced total mass (about $10^{-4} M_{\rm U}$). This result clearly solves the problem of a too massive and too compact impact-generated disk.

Once (sub-micrometre) icy grains condense in the disk, they coagulate with one another. In general, as the icy particles grow, the particles drift inward, pulled by the aerodynamic gas drag. However, the disk gas density is depleted so severely before the ice condensation that the growth is much faster than the drift and kilometre-sized "satellitesimals" are formed in situ without radial drift. Owing to the disk gas depletion, "type I migration" of proto-satellites caused by the torque from density waves in the disk would not be important, either. Therefore, the satellitesimals and satellites must be formed in situ.

3.2 N-body simulation

To investigate the satellite formation from a disk of solids with positive gradient, we performed three-dimensional N-body simulations from 10,000 bodies (satellitesimals) with individual masses $0.92 \times 10^{-8} M_{\rm U}$. Gravitational interactions of all the bodies, collisions and mergers are included. The calculation code for this simulation is same as Ishizawa et al. (2019) in Chapter 2. Aerodynamical gas drag to satellitesimals and type I migration due to disk-planet interactions are neglected. Tidal interactions with Uranus are also neglected, because the timescale of our run is too short for the effect to be important. Small eccentricities and inclinations are given initially. They are quickly relaxed by gravitational stirring and collision damping. We note that since there is no large reservoir of icy particles in the outer region of the disk and no

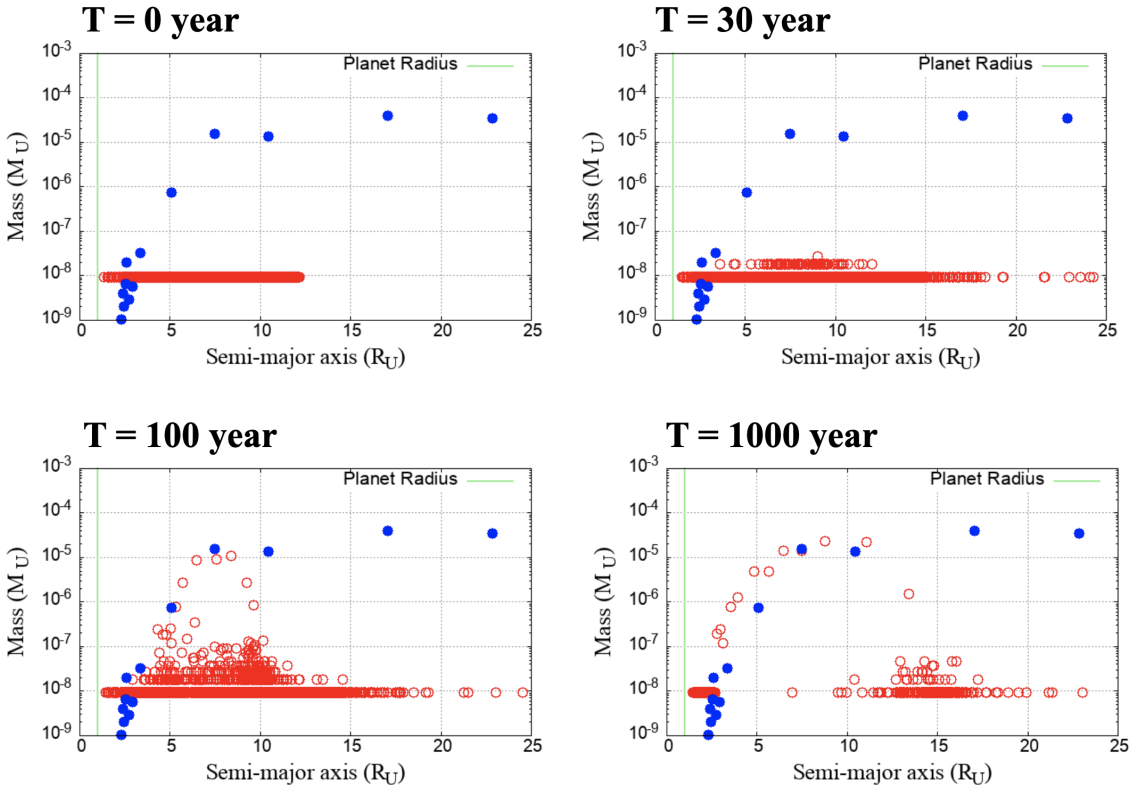

FIGURE 3.3: The time series of mass-orbit distributions of grown particles at 0, 30, 100, 1000 years in the calculation. The open red circles represent the result of N-body simulations with the predicted condensed ice surface density distribution given by Eq. (3.5) with $\beta = \gamma_{03} = 1$ and $r_{\rm max} \simeq 11\,R_{\rm U}$. The blue filled circles represent the regular satellites of Uranus.

icy particle supply from outside the Uranian system, pebble accretion is not effective and satellitesimals grow through mutual collisions. As the initial conditions of debris disks, the predicted ice distributions are given by Eq. (3.5) with $r_{\rm max} = 11R_{\rm U}, 20R_{\rm U}$ and $\beta = \gamma_{03} = 1$. The calculation in the case of $r_{\rm max} = 11R_{\rm U}$ is performed as a test case.

Figure 3.3 shows the time series of mass-orbit distributions of grown particles in the case of $r_{\rm max} \simeq 11R_{\rm U}$. After several tens of years, the particles at $r = 5 - 10R_{\rm U}$ begin to grow initially. After thousands of years, the particles inside $r = 15R_{\rm U}$ can reach the masses of the current satellites in the same regions, but the outer particles can't reach those of two outermost satellites, even if all satellitesimals in outer region accumulate to the outermost grown particle. This result suggests that when $r_{\rm max}$ does not reach to the orbit of the outermost satellite, Oberon, the mass-orbit distribution could not be reproduced through in-situ formation.

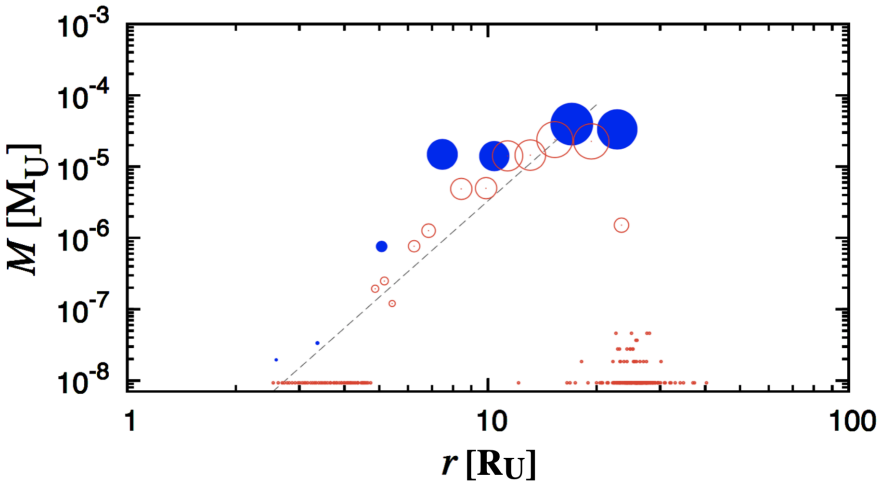

FIGURE 3.4: The mass-orbit distributions of grown particles at 2800 years in the calculation. The open red circles represent the result of N-body simulations with the predicted condensed ice surface density distribution given by Eq. (3.5) with $\beta = \gamma_{03} = 1$ and $r_{\rm max} \simeq 20\,R_{\rm U}$. The blue filled circles represent the regular satellites of Uranus.

Figure 3.4 shows the mass and orbital distribution of grown particles in the case of $r_{\rm max} \simeq 20 R_{\rm U}$, which is a feasible value from the past SPH simulations. The mass and orbital radius correlation is well reproduced. Although the number of accreted satellites is slightly larger in the simulation, some of the accreted satellites would collide with each other and small satellitesimals would be swept by the proto-satellites in a longer run, which would become consistent with the current major Uranian satellites. Because orbital migration of satellites is not important, the mass of accreted satellites is consistent with the isolation mass in oligarchic growth model (Kokubo & Ida, 2000), given by

$$\frac{m_{\rm iso}}{M_{\rm U}} \simeq 0.74 \times 10^{-4} \beta^{-3/2} \gamma_{03}^{3/2} \left(\frac{r}{20\,R_{\rm U}} \right)^{21/4} . \tag{3.9}$$

We also performed N-body simulations from ordinary $\Sigma_{\rm ice}$-distributions with a negative radial gradient and robustly showed that a positive gradient of $\Sigma_{\rm ice}$ is required to reproduce the current mass-orbit configuration (Ishizawa et al., 2019).

3.3 Discussion

3.3.1 Type I migration

When a proto-satellite grows, type I migration due to the torque from the density wakes in the gas disk becomes important. The migration timescale of a satellite with mass m is Tanaka et al. (2002),

$$t_{\rm mig} \sim \left(\frac{M_{\rm U}}{m}\right)\left(\frac{M_{\rm U}}{\Sigma_{\rm g} r^2}\right)\left(\frac{c_s}{v_{\rm K}}\right)^2 \Omega^{-1}. \tag{3.10}$$

For $c_s/v_{\rm K} \sim 0.05$, $m/M_{\rm U} \sim 3\times10^{-5}$, and $\Sigma_{\rm g} r^2/M_{\rm U} \sim 10^{-4}$, where we considered the most massive satellites and used the surface density of H/He gas as $(1-\gamma)\Sigma_{\rm g}$ at the ice condensation and at $r = 20\, r_{\rm U}$ (Eq. (B.20)), the type I migration timescale is $t_{\rm mig} \simeq 0.29(1-\gamma)^{-1}\times10^6\,\Omega^{-1}$. Because $t_{\rm diff} \sim 0.8\times10^6\,\Omega^{-1}$ and the H/He gas should decay more when the large enough satellites grow from satellitesimals, it is predicted that $t_{\rm mig} < t_{\rm diff}$. Furthermore, since $\Sigma_{\rm g} r^2 \sim m$, the disk gas may be modulated rather than the angular momentum of the proto-satellite is removed. Therefore, type I migration of a proto-satellite would not be efficient.

3.3.2 Condensation of silicate

The vaporization of rocks occurs at $T > 2{,}000$ K (Melosh, 2007). Owing to the high vaporization or condensation temperature, silicate (rock components) grains should quickly re-condense, while the disk is still massive and compact. Our model naturally produces an enhanced rock-to-ice ratio of the satellites because the ices condense after a reduction of water vapor by two orders of magnitude, whereas the rocks condense before substantial reduction has occurred. Although the silicates condense only in the inner region, they would also spread uniformly in the disk. Because silicate particles are not sticky at silicate-silicate collisions (Blum & Wurm, 2000), they do not grow larger than about 100μm and they radially spread with the turbulent viscous dissipation in the disk, unless the turbulence is very weak When collision velocity exceeds a threshold value (about 1 m/s), silicate-silicate collisional sticking is inhibited by rebounding or fragmentation. In the parameter range we consider, the particle collision velocity induced by turbulence is given by Eqs. (B.27) and (B.19). The maximum Stokes number of the particles that allows the sticking is

given by $v \simeq \Delta v$ as:

$$\mathrm{St}_{\max} \simeq \frac{1}{3\alpha}\left(\frac{v_{\mathrm{bf}}}{c_s \mathrm{s}}\right)^2 \tag{3.11}$$

$$\simeq 5\times10^{-4}\left(\frac{\alpha}{10^{-3}}\right)^{-1}\left(\frac{v_{\mathrm{bf}}}{1\mathrm{m/s}}\right)^2\left(\frac{\mu_{\mathrm{g}}}{2.8}\right)\left(\frac{T}{240\mathrm{K}}\right)^{-1} \tag{3.12}$$

Thus, silicates can grow only up to $\mathrm{St} \simeq 5\times10^{-4}$ until T deceases to the ice condensation temperature of about 240 K. In the Stokes drag regime, it corresponds to a particle size of around 100 μm. The silicate particles can form satellitesimals only after ices condense and they stick to the icy particles or ices condense to their surface.

3.3.3 Application to other systems

Although we have focused on Uranus, the model here provides a general scenario for satellite formation around ice giants with scaling by the mass and the physical radius of a central planet, which is completely different from satellite-formation scenarios around terrestrial planets and gas giants. It could also be applied to the inner region of Neptune's satellite system, where we can neglect the effect of Triton that may have been captured (Agnor & Hamilton, 2006). Observations suggest that many of the super-Earths discovered in exoplanetary systems may consist of abundant water ice, even in close-in (warm) orbits. The model here may also provide insights into possible icy satellites of super-Earths.

Chapter 4

Summary

We investigated the formation process of the Uranian satellites from a disk generated by a giant impact to examine whether the current satellites could have been formed in situ through a giant impact. We modeled a wide debris disk generated by the giant impact, performed N-body simulations of satellites accretion in such a disk, and investigated the feasibility of the in-situ formation of the Uranian satellites, taking into account the orbital evolution of satellites due to the planetary tides after their growth. In such a disk the surface density varies as $\Sigma \propto r^{-q}$ with $q \sim 1.5$ with respect to the radial distance from Uranus. We then found that satellites in the middle region ($3R_{\rm U}$ to $13R_{\rm U}$) would have much larger masses than Ariel or Umbriel, whereas the outermost satellite would not obtain a mass of Oberon; that is, the orbital distribution of the five major satellites could not be reproduced.

We still believe, however, that the five major satellites have formed in the current site, since it would be difficult to form from rings inside the Roche limit. We then noticed that an evaporated disk after a giant impact should experience thermal and viscous evolution.

When we properly considered such viscous evolution of the evaporated disk, we found through one-dimensional viscous diffusion simulations that an impact-generated compact disk is quickly relaxed to a quasi-steady accretion disk and its surface density and temperature evolution are approximated by an analytical self-similar formula. We also found that the circumplanetary disk of the condensed ice could have negative q value with very weak dependence on the initial condition determined by the impact parameters. We performed the N-body simulations with the predicted ice distribution, finding finally that the current Uranian major satellites

could well be reproduced by the N-body simulation. as shown in Fig. 3.4. To conclude, it is feasible to explain the origin of the Uranian satellites through a giant impact.

Appendix A

A.1 Separation between two colliding particles

When the distance between two particles is smaller than or equal to the sum of their radii, the collision is detected. If the distance between two particles is still smaller than the sum of their radii in the next time step, an unnecessary additional collision can be detected by mistake. In order to avoid such unnecessary collision detections, two particles should be separated for the distance between them to be equal to the sum of their radii on the basis of conservation of angular momentum.

Hereafter two colliding particles, particle i and particle j, are considered. First, after two particles collide with each other, their velocities are changed based on Eqs.(2.4), (2.5) and conservation of momentum as given by

$$m_i \boldsymbol{v}_{\boldsymbol{i}}' + m_j \boldsymbol{v}_{\boldsymbol{j}}' = m_i \boldsymbol{v}_{\boldsymbol{i}} + m_j \boldsymbol{v}_{\boldsymbol{j}}, \tag{A.1}$$

where m, $\boldsymbol{v}$ and $\boldsymbol{v}'$ are mass, impact velocity, and rebound velocity of a particle, respectively. The subscripts represent a kind of particles, i or j. Figure A.1 shows a sketch of a collision, where $\boldsymbol{v_{ij}} = \boldsymbol{v_j} - \boldsymbol{v_i}$ and $\boldsymbol{v_{ij}'} = \boldsymbol{v_j'} - \boldsymbol{v_i'}$.

Second, a separation between of two particles after a collision is carried out based on conservation of angular momentum,

$$m_i \boldsymbol{r}_{\boldsymbol{i}}' \times \boldsymbol{v}_{\boldsymbol{i}}' + m_j \boldsymbol{r}_{\boldsymbol{j}}' \times \boldsymbol{v}_{\boldsymbol{j}}' = m_i \boldsymbol{r}_{\boldsymbol{i}} \times \boldsymbol{v}_{\boldsymbol{i}}' + m_j \boldsymbol{r}_{\boldsymbol{j}} \times \boldsymbol{v}_{\boldsymbol{j}}', \tag{A.2}$$

where $\boldsymbol{r}$ and $\boldsymbol{r}'$ indicate orbital radii of particles before and after a separation, respectively, and also based on the following equations;

$$\boldsymbol{r_{ij}'} = \boldsymbol{r_{ij}} + \boldsymbol{x_{ij}}, \tag{A.3}$$

$$\boldsymbol{x_{ij}} \parallel \boldsymbol{v_{ij}'}, \tag{A.4}$$

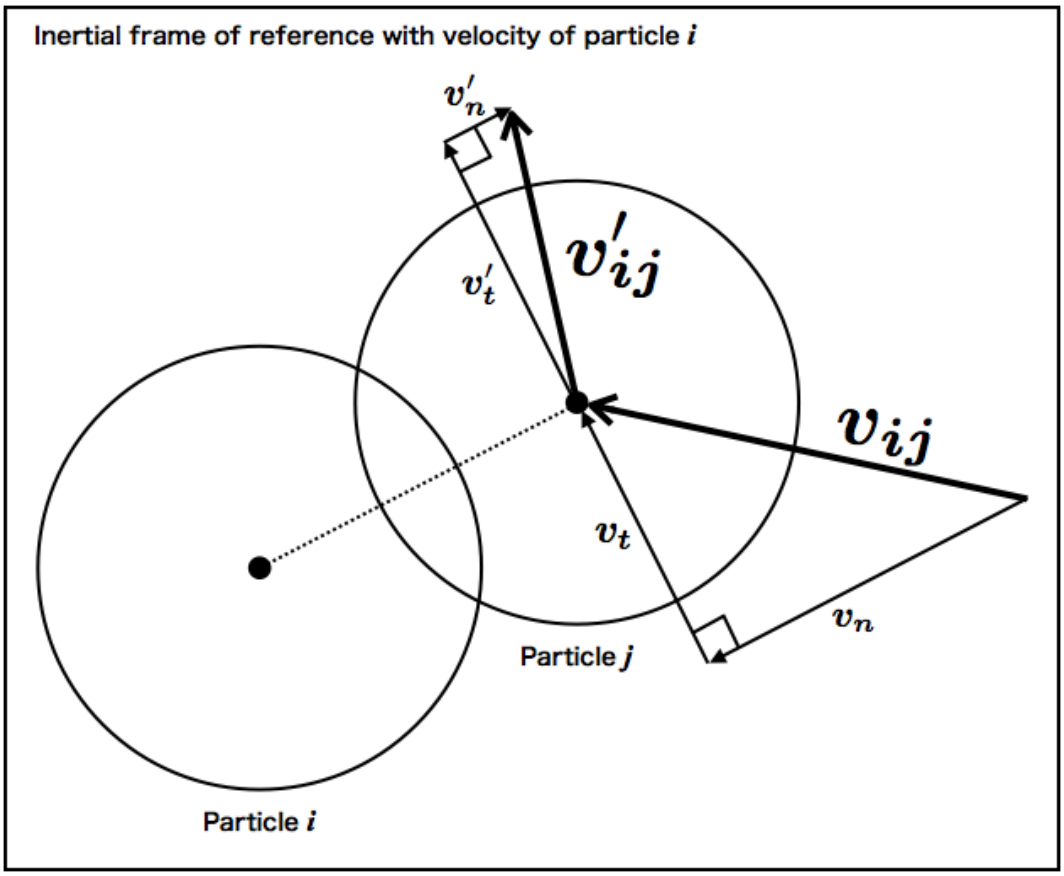

FIGURE A.1: A sketch of a rebound between two colliding particles in the inertial frame of reference with the impact velocity of particle i.

where $\boldsymbol{r_{ij}} = \boldsymbol{r_j} - \boldsymbol{r_i}$, $\boldsymbol{r'_{ij}} = \boldsymbol{r'_j} - \boldsymbol{r'_i}$, and $\boldsymbol{x_{ij}}$ is a modifying vector as represented in Fig.A.2, which is set to be parallel to the relative rebound velocity.

Then $\boldsymbol{x_{ij}}$ is determined by,

$$\boldsymbol{x_{ij}} = \left(-\frac{\boldsymbol{r_{ij}} \cdot \boldsymbol{v_{ij}}}{|\boldsymbol{v_{ij}}|} + \sqrt{\left(\frac{\boldsymbol{r_{ij}} \cdot \boldsymbol{v_{ij}}}{|\boldsymbol{v_{ij}}|} \right)^2 + r_{\mathrm{p}ij}^2 - |\boldsymbol{r_{ij}}|^2} \right) \frac{\boldsymbol{v_{ij}}}{|\boldsymbol{v_{ij}}|}, \tag{A.5}$$

where $r_{\mathrm{p}ij}$ is the sum of the particles' radii.

Finally, each modified orbital radius $\boldsymbol{r'}$ is given by,

$$\alpha_{ij} = \frac{m_i(\boldsymbol{x_{ij}} \times \boldsymbol{v'_j}) \cdot (\boldsymbol{x_{ij}} \times \boldsymbol{v'_i})}{m_j |\boldsymbol{x_{ij}} \times \boldsymbol{v'_j}|^2}, \tag{A.6}$$

$$\boldsymbol{r'_i} = \boldsymbol{r_i} - \frac{1}{\alpha_{ij} + 1} \boldsymbol{x_{ij}}, \tag{A.7}$$

$$\boldsymbol{r'_j} = \boldsymbol{r_j} + \frac{\alpha_{ij}}{\alpha_{ij} + 1} \boldsymbol{x_{ij}}. \tag{A.8}$$

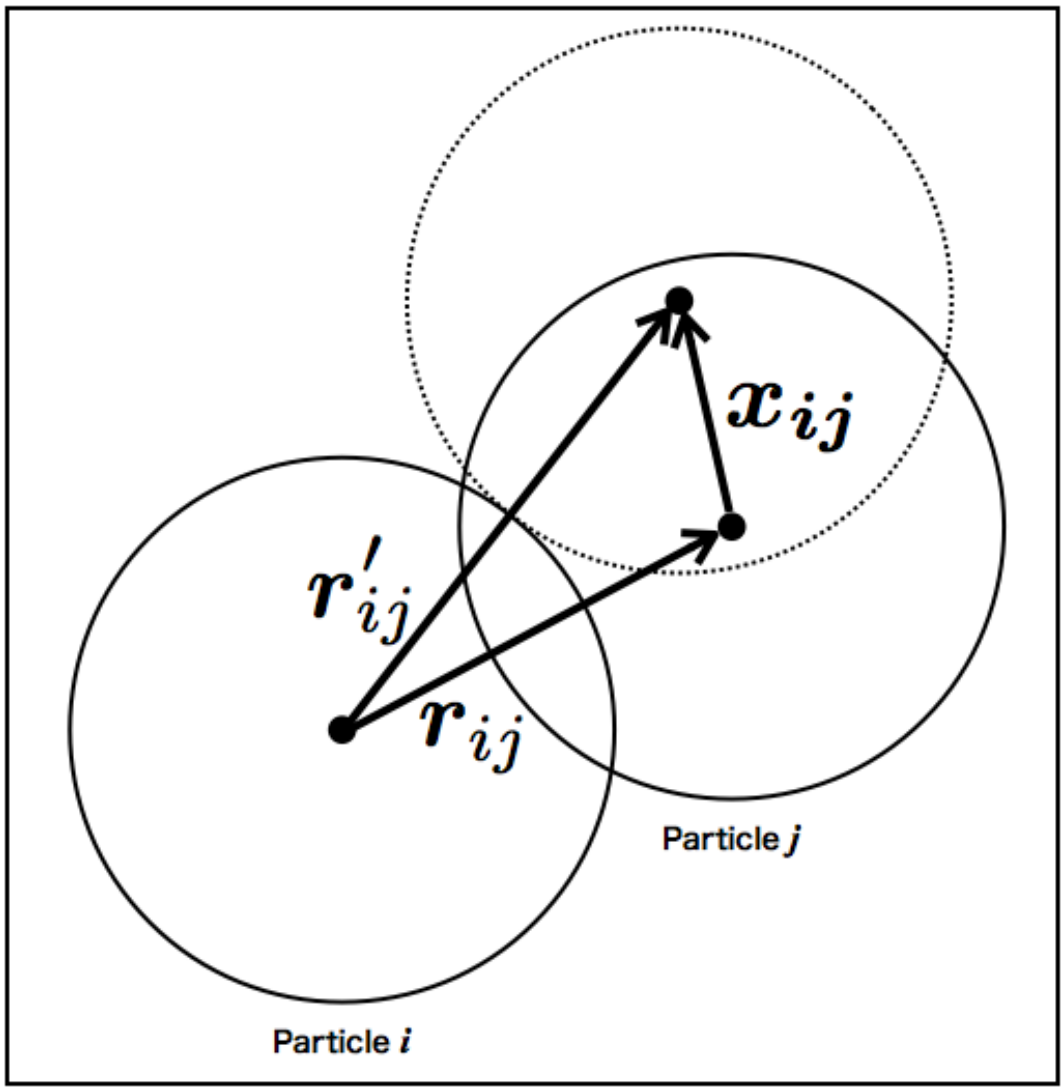

FIGURE A.2: A sketch of a separating two particles.

A.2 Isolation mass

The isolation mass, $M_{\rm iso}$, is the asymptotic mass derived from the basic analysis model when neglecting the radial diffusion and orbital evolution of the satellites. It is expressed by the following equation with reference to the core accretion model of planetary formation (e.g. Lissauer 1987; Kokubo & Ida 1998, 2000):

$$M_{\rm iso} = 2\pi a \cdot 10 r_{\rm H} \cdot \Sigma, \tag{A.9}$$

where Σ is the surface density of satellitesimals, which is given by

$$\Sigma = \frac{M_{\rm disk}}{\int_{a_{\rm min}}^{a_{\rm max}} 2\pi a^{1-q} {\rm d}a} a^{-q}, \tag{A.10}$$

and $r_{\rm H}$ is the Hill radius of an isolation mass, which is given by $(2M_{\rm iso}/3M_{\rm U})^{1/3}$. Therefore,

$$M_{\rm iso} \simeq \begin{cases} 0.26 \times \left[\dfrac{2-q}{a_{\rm max}^{2-q} - a_{\rm min}^{2-q}}\right]^{\frac{3}{2}} \left(\dfrac{M_{\rm disk}}{M_{\rm tot}}\right)^{\frac{3}{2}} \left(\dfrac{a}{a_{\rm R}}\right)^{\frac{3}{2}(2-q)} M_{\rm tot} & (q \neq 2) \\ 0.26 \times \left[\ln\left(\dfrac{a_{\rm max}}{a_{\rm min}}\right)\right]^{-\frac{3}{2}} \left(\dfrac{M_{\rm disk}}{M_{\rm tot}}\right)^{\frac{3}{2}} M_{\rm tot} & (q = 2) \end{cases}, \tag{A.11}$$

where $a_{\rm max}$ and $a_{\rm min}$ are the semimajor axes of the outer and the inner edge of a satellite-forming disk, respectively. Eq.(A.11) indicates that if $q > 2$, the isolation mass increases with the semimajor axis, whereas if $q < 2$, the isolation mass decreases with the semimajor axis. If $q = 2$, the isolation mass does not depend on the semimajor axis.

Appendix B

B.1 Analytical solution to viscous diffusion equation

The analytical self-similar solution to the one-dimensional viscous diffusion equation (Eq. 3.3) is given by (Lynden-Bell & Pringle, 1974; Hartmann et al., 1998)

$$\Sigma_{\rm g} \propto t_*^{-(5/2-\zeta)/(2-\zeta)} r^{-\zeta} \exp\left[-\left(\frac{r}{r_{\rm d,0}}\right)^{2-\zeta} t_*^{-1}\right]. \tag{B.1}$$

where $\zeta = d\ln\nu/d\ln r$, $t_* = 1 + t/t_{\rm diff}$, and

$$t_{\rm diff} = \frac{1}{3(2-\zeta)^2}\left(\frac{r^2}{\nu}\right)_{r_{\rm d,0}}, \tag{B.2}$$

where subscript $r_{\rm d,0}$ indicates the value at $r_{\rm d,0}$. The surface density is $\propto r^{-\zeta}$ for $r \ll r_{\rm d,0}$ and exponentially decays for $r \gtrsim r_{\rm d} = r_{\rm d,0}\, t_*^{1/(2-\zeta)}$, so that $r_{\rm d}$ is the characteristic disk radius and $r_{\rm d,0}$ is the value when the impact-generated disk is relaxed to the quasi-steady self-similar solution ($t = 0$).

In the case of their simple viscous heating model, $\nu \sim \alpha c_s^2/\Omega \propto T\, r^{3/2} \propto \Sigma_{\rm g}^{1/3}\, r$. In inner disk regions, the disk accretion is steady and its rate is independent of r, that is, $\Sigma_{\rm g}\nu$ is independent of r. In this case, $T \propto r^{-3/4}$ by Eq. (3.1), so $\nu \propto c_s^2\Omega^{-1} \propto Tr^{3/2} \propto r^{3/4}$. With $\zeta = 3/4$, the self-similar solution given by Eq. (B.1) is

$$\Sigma_{\rm g} = \Sigma_{\rm g,0}\, t_*^{-7/5}\left(\frac{r}{R_{\rm U}}\right)^{-3/4} \exp\left[-\left(\frac{r}{r_{\rm d,0}}\right)^{5/4} t_*^{-1}\right], \tag{B.3}$$

where $R_{\rm U}$ is the Uranian physical radius, and $\Sigma_{\rm g,0}$ is the initial disk surface density $r = R_{\rm U}$.

In the original self-similar solution, $t_{\rm diff}$ (Eq. (B.2)) is a constant with time. However, in our case, $\nu \propto \Sigma_{\rm g}^{1/3}$ derived by Eq. (3.1) and Eq. (3.2). As the disk viscously

expands and $\Sigma_{\rm g}$ decreases, ν at $r = r_{\rm d,0}$ in Eq. (B.2) also decreases. As a result, $t_{\rm diff}$ increases. Because we are concerned with $t > t_{\rm diff}$, $t_* \propto t_{\rm diff}^{-1} \propto \nu \propto \Sigma_{\rm g}^{1/3}$. Taking this effect into account, Eq. (B.3) suggests $\Sigma_{\rm g} \propto t_{*,0}^{-7/5} \Sigma_{\rm g}^{(-7/5)\times(1/3)}$, where $t_{*,0} = 1 + t/t_{\rm diff,0}$, and $t_{\rm diff,0}$ is defined by quantities at $t = 0$ as (Eq. (B.2) with $\zeta = 3/4$)

$$t_{\rm diff,0} = \frac{16}{75} \left(\frac{r^2}{\nu} \right)_{r_{\rm d,0}, t=0}. \tag{B.4}$$

From $\Sigma_{\rm g} \propto t_{*,0}^{-7/5} \Sigma_{\rm g}^{(-7/5)\times(1/3)}$, $\Sigma_{\rm g} \propto t_{*,0}^{-21/22}$ and t_* at $t > 0$ is $\propto t_{*,0} \Sigma_{\rm g}^{1/3} \propto t_{*,0}^{15/22}$. Thereby, the final formula is

$$\Sigma_{\rm g} = \Sigma_{\rm g,0}\, t_{*,0}^{-21/22} \left(\frac{r}{R_{\rm U}} \right)^{-3/4} \exp\left[- \left(\frac{r}{r_{\rm d,0}} \right)^{5/4} t_{*,0}^{-15/22} \right], \tag{B.5}$$

$$t_{*,0} = 1 + t/t_{\rm diff,0}. \tag{B.6}$$

Although this formula is no longer a strict self-similar solution, it reproduces the numerical solution well, as shown in Fig. 3.1 with dashed lines.

The parameters $r_{\rm d,0}$ and $\Sigma_{\rm g,0}$ in the analytical formula can be estimated by the total mass ($M_{\rm d,imp}$) and the angular momentum ($j_{\rm d,imp}$) of the impact-generated disk. In general, SPH simulations show that the impact-generated disk is centrally-concentrated and the mean radius is $\langle r_{\rm d,imp} \rangle \sim 2R_{\rm U}$ (Slattery et al., 1992; Kegerreis et al., 2018), where $\langle r_{\rm d,imp} \rangle$ is defined with the specific angular momentum, $j_{\rm d,imp} = J_{\rm d,imp}/M_{\rm d,imp}$, by $\langle r_{\rm d,imp} \rangle = (j_{\rm d,imp}/R_{\rm U}^2 \Omega_{\rm U})^2 R_{\rm U}$. The value of $\langle r_{\rm d,imp} \rangle$ is larger for less steep radial gradient of the disk surface density. In the SPH impact simulations, debris particles generally have eccentric orbits. However, since the orbits should be eventually circularized, conserving angular momentum, we define $\langle r_{\rm d,imp} \rangle$ with the assumption that the orbits are circular.

Because the radial gradient of the disk surface density is generally very steep, the disk expands to a quasi-steady distribution, almost keeping the total disk angular momentum. While the total angular momentum is conserved, innermost disk gas generally tends to spiral in by losing angular momentum. The one-dimensional diffusion simulations here show that a half of the mass inside the mean radius in the impact-generated disk falls onto the planet before the gas surface density distribution settles down to the quasi-steady self-similar solution. If we consider the disk surface density distribution just after the impact as $\Sigma_{\rm g} \propto r^{-3}$ with a truncation at $r = 10R_{\rm U}$,

which is suggested by SHP simulations, the initial mass of the impact-generated disk ($M_{\rm d,imp}$) is decreased by $\sim 20\%$ when the disk relaxed to the quasi-steady state. Using $j_{\rm d,imp}$ of the impact-generated disk and the modified disk mass $0.8M_{\rm d,imp}$, we can evaluate $r_{\rm d,0}$ and $\Sigma_{\rm g,0}$ in the analytical self-similar formula for the quasi-steady state as follows.

The initial total disk mass and angular momentum of the analytical formula are

$$\begin{aligned} M_{\rm d,ss} &= \int_{R_{\rm U}}^{\infty} 2\pi r\Sigma_{\rm g} dr = \frac{8\pi}{5} R_{\rm U}^2 \Sigma_{\rm g,0} \left(\frac{r_{\rm d,0}}{R_{\rm U}}\right)^{5/4} e^{-(r_{\rm d,0}/R_{\rm U})^{-5/4}} \\ &\simeq \frac{8\pi}{5} R_{\rm U}^2 \Sigma_{\rm g,0} \left(\frac{r_{\rm d,0}}{R_{\rm U}}\right)^{5/4} \times 0.776, \qquad \text{(B.7)} \\ J_{\rm d,ss} &= \int_{R_{\rm U}}^{\infty} 2\pi r\Sigma_{\rm g} \sqrt{GM_{\rm U} r}\, dr = \frac{8\pi}{5} R_{\rm U}^4 \Omega_{\rm U} \Sigma_{\rm g,0} \left(\frac{r_{\rm d,0}}{R_{\rm U}}\right)^{7/4} \Gamma\left(\frac{7}{5}, \left(\frac{r_{\rm d,0}}{R_{\rm U}}\right)^{-5/4}\right) \\ &\simeq \frac{8\pi}{5} R_{\rm U}^4 \Sigma_{\rm g,0} \Omega_{\rm U} \left(\frac{r_{\rm d,0}}{R_{\rm U}}\right)^{7/4} \times 0.797, \qquad \text{(B.8)} \end{aligned}$$

where Γ is a 2nd-kind incomplete gamma function, $\Omega_{\rm U}$ is the disk orbital frequency at $r = R_{\rm U}$, and we used $r_{\rm d,0}/R_{\rm U} \sim 3$ to evaluate $e^{-(r_{\rm d,0}/R_{\rm U})^{-5/4}}$ and $\Gamma\left(\frac{7}{5}, (r_{\rm d,0}/R_{\rm U})^{-5/4}\right)$.

From Eqs. (B.7) and (B.8), the mean specific angular momentum of the analytical formula is given by

$$j_{\rm d,ss} \simeq \frac{J_{\rm d,ss}}{M_{\rm d,ss}} = 1.03 \left(\frac{r_{\rm d,0}}{R_{\rm U}}\right)^{1/2} \Omega_{\rm U} R_{\rm U}^2. \qquad \text{(B.9)}$$

Because $j_{\rm d,ss} = J_{\rm d,ss}/M_{\rm d,ss} \simeq J_{\rm d,imp}/0.8M_{\rm d,imp} \simeq 1.25\, j_{\rm d,imp}$,

$$r_{\rm d,0} \simeq 1.47 \left(\frac{j_{\rm d,imp}}{R_{\rm U}^2 \Omega_{\rm U}}\right)^2 R_{\rm U} = 1.47 \langle r_{\rm d,imp} \rangle. \qquad \text{(B.10)}$$

From Eq. (B.7) with $M_{\rm d,ss} \sim 0.8\, M_{\rm d,imp}$, the initial surface density of the quasi-steady disk after the viscous relaxation of the impact-generated disk is

$$\begin{aligned} \Sigma_{\rm g,0} &\simeq 0.256 \left(\frac{r_{\rm d,0}}{R_{\rm U}}\right)^{-5/4} \left(\frac{M_{\rm d,ss}}{R_{\rm U}^2}\right) \\ &\simeq 6.5 \times 10^7 \left(\frac{\langle r_{\rm d,imp} \rangle}{2\, R_{\rm U}}\right)^{-5/4} \left(\frac{M_{\rm d,imp}}{10^{-2} M_{\rm U}}\right) \ {\rm kg/m^2}. \qquad \text{(B.11)} \end{aligned}$$

In the case of the impact disk with $\Sigma_{\rm g} = \Sigma_{\rm g,imp0}(r/R_{\rm U})^{-3}$ with a truncation at $r = 10\, R_{\rm U}$, $M_{\rm d,imp} = 0.9 \times 2\pi\Sigma_{\rm g,imp0} R_{\rm U}^2$ and $j_{\rm d,imp} = 1.5\, R_{\rm U}^2 \Omega_{\rm U}$, so that $r_{\rm d,0} \simeq 3.3\, R_{\rm U}$

and $\Sigma_{g,0} \simeq 0.26\,\Sigma_{g,imp0}$. These condition is used for calculations of the analytical distribution of the water vapor disk as shown in Fig. 3.1

To evaluate the outer limit of the ice condensation, the envelope curve of superposition of Σ_g-r curves at all the different times is important. The Σ_g-distribution of the analytical solution starts exponentially declining at $r_d \sim r_{d,0} t_*^{12/22}$ and the absolute vales of Σ_g at the same r scales by $t_*^{-21/22}$, while Σ_g further decreases proportional to $r_d^{-3/4} \propto t_*^{-9/22}$, as shown in Eq. (B.5). Therefore, the envelope curve is given by

$$\Sigma_{g,env} \simeq \Sigma_{g,0} \left(\frac{r}{R_U}\right)^{-[(21+9)/22]/(12/22)} \tag{B.12}$$

$$\simeq 6.5 \times 10^7 \left(\frac{\langle r_{d,imp}\rangle}{2\,R_U}\right)^{-5/4} \left(\frac{M_{disk}}{10^{-2} M_U}\right) \left(\frac{r}{R_U}\right)^{-5/2} \text{ kg/m}^2. \tag{B.13}$$

The intersection radius between $\Sigma_{g,env}$ and Σ_g at the ice condensation (Eq. (B.20)) is given by

$$r_{max} \simeq 20 \left[\beta \left(\frac{\langle r_{d,imp}\rangle}{2\,R_U}\right)^{-5/4} \left(\frac{M_{disk}}{10^{-2} M_U}\right)\right]^{1/4} R_U. \tag{B.14}$$

B.2 Ice condensation temperature

Icy grains condense when the vapor pressure exceeds the vapor saturation pressure. Because the vapor saturation pressure depends sensitively on temperature, the condensation condition is often described by $T < T_{ice}$, where T_{ice} is the condensation temperature given by (Lichtenegger & Komle, 1991)

$$T_{ice} \simeq \frac{A}{B - \log_{10}(P_{H2O}[\text{Pa}])} \text{ [K]} \tag{B.15}$$

with

$$A \simeq 2633\ ;\ B \simeq 12.06, \tag{B.16}$$

where P_{H2O} is the partial pressure of water vapor in the disk, given by

$$P_{H2O} = \gamma \frac{\mu_g}{\mu_{H2O}} P \simeq 0.156\,\gamma\,P, \tag{B.17}$$

where P is the total pressure, $\gamma = \Sigma_{H2O}/\Sigma_g$, and $\mu_g \simeq 2.8\ \gamma$ is the abundance of water vapor in the disk and $\mu_{H2O} = 18$, which is H_2O mean molecular weight.

The total pressure is

$$\begin{aligned} P &= \rho_{\rm g} c_s^2 = \frac{\Sigma_{\rm g}}{\sqrt{2\pi}} c_s \Omega \\ &\simeq 61.9 \left(\frac{\alpha}{10^{-3}}\right)^{-1} \left(\frac{T}{240\,{\rm K}}\right)^{7/2} \ {\rm Pa}, \end{aligned} \tag{B.18}$$

where we used

$$c_s \simeq 8.41 \times 10^2 (\mu_g/2.8)^{-1/2} (T/240{\rm K})^{1/2} \ {\rm m/s} \tag{B.19}$$

and $\Sigma_{\rm g}$ obtained by Eq. (3.1),

$$\Sigma_{\rm g} \simeq 4.02 \times 10^2 \left(\frac{\alpha}{10^{-3}}\right)^{-1} \left(\frac{T}{240\,{\rm K}}\right)^{3} \left(\frac{r}{R_{\rm U}}\right)^{3/2} \ [{\rm kg/m^2}]. \tag{B.20}$$

This $\Sigma_{\rm g}$ means Thereby,

$$P_{\rm H2O} = 0.156\,\gamma P \simeq 9.66\gamma \left(\frac{\alpha}{10^{-3}}\right)^{-1} \left(\frac{T}{240\,{\rm K}}\right)^{7/2} \ {\rm Pa}, \tag{B.21}$$

Substituting $P_{\rm H2O}$ in Eq. (B.21) to Eq. (B.15) with $T = T_{\rm ice}$, we found

$$\begin{aligned} T_{\rm ice} &\simeq \frac{2633}{12.06 - 0.98 - \log_{10}\left[\frac{\gamma}{0.3}\left(\frac{\alpha}{10^{-3}}\right)^{-1}\right]} \ {\rm K} \\ &\simeq \frac{238}{1 - \frac{1}{11.08}\log_{10}\left[\frac{\gamma}{0.3}\left(\frac{\alpha}{10^{-3}}\right)^{-1}\right]} \ {\rm K} \\ &\simeq 238 + 21 \log_{10}\left[\frac{\gamma}{0.3}\left(\frac{\alpha}{10^{-3}}\right)^{-1}\right] \ {\rm K}. \end{aligned} \tag{B.22}$$

Note that the r-dependence vanishes for $T_{\rm ice}$ in our disk model.

B.3 Comparison of timescales

Here we show that the disk gas density has significantly decayed before the ice condensation and that the timescale of radial drift of the condensed icy particles is much longer than their growth timescale. The growth timescale is also much shorter than the gas disk diffusion timescales. Thereby, the condensed icy grains quickly grow to km-sized “satellitesimals," which are building blocks of satellites, in situ in the H/He gas disk.

Disk diffusion timescale:

We consider a disk with a characteristic radius of $r_{\rm d,0}$ and a turbulent viscosity of $\alpha c_s^2 \Omega^{-1}$, where c_s is the local sound velocity of the disk gas, Ω is the local orbital frequency of the gas, and α is a parameter to represent the strength of turbulence ($\alpha \ll 1$) (Shakura & Sunyaev, 1973). From the disk radial diffusion equation Eq. (B.2), the characteristic diffusion timescale in the case of $\nu \propto r^{3/4}$ is given by (Eq. (B.4))

$$\tau_{\rm diff} \sim \frac{16\, r_{\rm d,0}^2}{75\, \nu} \sim \frac{16}{75\, \alpha} \left[\left(\frac{c_s}{v_{\rm K}} \right)^{-2} \Omega^{-1} \right]_{r_{\rm d,0}}, \tag{B.23}$$

where $v_{\rm K} \simeq r\Omega$ is Keplerian velocity.

Drift timescale of icy particles due to gas drag:

The condensed icy grains coagulate with each other. As the icy particles grow, their motions become less coupled to the disk gas. The degree of the decoupling is represented by Stokes number, $\mathrm{St} = t_{\rm stop}\Omega$, where $t_{\rm stop}$ is the stopping time due to aerodynamic gas drag. The disk gas rotates slower than the particles by a small fraction of $\eta \sim (c_s/v_{\rm K})^2$ ($\ll 1$), because of radial pressure gradient, the particles drift inward with the drift timescale given by (Nakagawa et al., 1986):

$$\tau_{\rm drift} \sim \frac{r}{v_r} \sim \frac{r}{2\eta\, v_{\rm K}} \frac{1+\mathrm{St}^2}{\mathrm{St}} \sim 0.5 \left(\frac{c_s}{v_{\rm K}} \right)^{-2} \frac{1+\mathrm{St}^2}{\mathrm{St}} \Omega^{-1}, \tag{B.24}$$

where v_r is the radial drift velocity. The drift is the fastest at $\mathrm{St} \sim 1$.

Growth timescale of icy particles:

The growth times scale (mass-doubling timescale) is given by

$$\tau_{\rm grow} \sim \frac{1}{n\pi R^2 \Delta v}, \tag{B.25}$$

where R is the particle physical radius, n is their spatial number density,

$$n = \frac{\rho_{\rm p}}{(4\pi/3)\rho_{\rm mat} R^3}, \tag{B.26}$$

$\rho_{\rm p}$ and $\rho_{\rm mat}$ are the spatial and material densities of the particles and Δv is the relative velocity between the particles (Ormel & Cuzzi, 2007),

$$\Delta v \simeq \left(\frac{3\alpha\,{\rm St}}{1+{\rm St}^2}\right)^{1/2} c_s, \tag{B.27}$$

The icy particle spatial density is given by their surface density $\Sigma_{\rm ice}$ as (Dubrulle et al., 1995)

$$\rho_{\rm p} \simeq \frac{\Sigma_{\rm ice}}{\sqrt{2\pi}h_{\rm p}} \simeq \frac{\Sigma_{\rm ice}}{\sqrt{2\pi}h_{\rm g}}\left(1+\frac{\rm St}{\alpha}\right)^{1/2}, \tag{B.28}$$

where $h_{\rm p}$ and $h_{\rm g}$ are the particle and the gas vertical scale heights. Substituting Eqs. (B.26), (B.27), and (B.28) into Eq. (B.25), we obtain

$$\tau_{\rm grow} \sim \frac{4\sqrt{2\pi}}{3\sqrt{3}}\frac{\rho_{\rm mat}R}{\sqrt{{\rm St}({\rm St}+\alpha)}\,\Sigma_{\rm ice}}\Omega^{-1}, \tag{B.29}$$

where we used the disk gas scale height is given by $h_{\rm g} \sim c_s\Omega^{-1}$.

In the situation we are considering, the drag law is mostly in Stokes drag regime. In this case, the Stokes number is given by

$${\rm St} \sim \frac{4\rho_{\rm mat}\sigma_{\rm coll}R^2\Omega}{9\mu_{\rm HHe}\,m_{\rm H}\,c_s} \sim 1.5\times10^{-6}\left(\frac{T_{\rm ice}}{240\,{\rm K}}\right)^{-1/2}\left(\frac{R}{\mu{\rm m}}\right)^2\left(\frac{r}{R_{\rm U}}\right)^{-3/2}, \tag{B.30}$$

where we used $\rho_{\rm mat} \sim 10^3$ [kg/m^3], $\mu_{\rm HHe} \sim 2.4$ is the mean molecular weight for H-He gas, $m_{\rm H} \sim 1.67\times10^{-21}$kg is the hydrogen mass, and $\sigma_{\rm col} \sim 2\times10^{-11}$m^2 is the collision cross section. Substituting Eqs. (B.30) and (3.5) into Eq. (B.29), we obtain

$$\tau_{\rm grow} \sim 1\left(\frac{{\rm St}+\alpha}{10^{-4}}\right)^{-1/2}\left(\frac{\gamma}{0.3}\right)^{-1}\left(\frac{\alpha}{10^{-4}}\right)\left(\frac{T_{\rm ice}}{240\,{\rm K}}\right)^{-11/4}\left(\frac{r}{R_{\rm U}}\right)^{-3/4}\Omega^{-1}. \tag{B.31}$$

Timescale comparison:

Because $c_s \ll v_{\rm K}$ and $\alpha \ll 1$,

$$\tau_{\rm grow} \ll \tau_{\rm drift}, \tau_{\rm diff}. \tag{B.32}$$

Around ${\rm St} \sim 1$,

$$\tau_{\rm grow} \ll \tau_{\rm drift} \ll \tau_{\rm diff}. \tag{B.33}$$

These results imply that the condensed icy grains quickly grow to km-sized satellitesimals in situ in the H/He gas disk. The satellitesimal motions are decoupled from the disk gas.

Bibliography

Agnor, C. B. & Hamilton, D. P. 2006, Nature, 441, 192

Blum, J. & Wurm, G. 2000, Icarus, 143, 138

Boué, G. & Laskar, J. 2010, ApJ, 712, L44

Canup, R. M. & Asphaug, E. 2001, Nature, 412, 708

Canup, R. M. & Ward, W. R. 2002, AJ, 124, 3404

Canup, R. M. & Ward, W. R. 2006, Nature, 441, 834

Charnoz, S., Salmon, J. & Crida, A. 2010, Nature, 465, 752

Crida, A. & Charnoz, S. 2012, Science, 338, 1196

Daisaka, H., Tanaka, H. & Ida, S. 2001, Icarus, 154, 296

Dermott, S. F., Malhotra, R., & Murray, C. D. 1988, Icarus, 76, 295

Dubrulle, B., Morfill, G., & Sterzik, M. 1995, Icarus, 114, 237

Gavrilov, S. V. & Zharkov, V. N. 1977, Icarus, 32, 443

Hartmann, L., Calvet, N., Gullbring, E., et al. 1998, ApJ, 495, 385

Hesselbrock, A. J., Minton, D. A. 2019, ApJ, 157, 30

Hyodo, R., Ohtsuki, K. & Takeda, T. 2015, ApJ, 799, 40

Ishizawa, Y., Sasaki, T. & Hosono, N. 2019, ApJ, 885, 132

Ida, S., Canup, R. M., & Stewart, G. R. 1997, Nature, 389, 353

Ida, S., Ueta, S., Sasaki, T. & Ishizawa, Y. 2019, Nature Astronomy, 4, 880-885

Iwasawa, M., Tanikawa, A., Hosono, N., et al. 2016, PASJ, 68, 54

Kegerreis, J. A., Teodoro, L. F. A., Eke, V. R., et al. 2018, ApJ, 861, 52

Kokubo, E. & Ida, S. 1998, Icarus, 131, 171

Kokubo, E. & Ida, S. 2000, Icarus, 143, 15

Kokubo, E., Ida, S., & Makino, J. 2000, Icarus, 148, 419

Lichtenegger, H. I. M. & Komle, N. I. 1991, Icarus, 90, 319

Lissauer, J. J. 1987, Icarus, 69, 249

Lissauer, J. J. & Stewart, G. R. 1993, Protostars and Planets III, 1061

Lynden-Bell, D. and Pringle, J.E. 1974, MNRAS, 168, 603

Makino, J. & Aarseth, S. J. 1992, PASJ, 44, 141

Melosh, H. J. 2007, Meteoritics and Planetary Science, 42, 2079

Morbidelli, A., Tsiganis, K., Batygin, K., et al. 2012, Icarus, 219, 737

Nakagawa, Y., Sekiya, M., & Hayashi, C. 1986, Icarus, 67, 375

Ormel, C. W. & Cuzzi, J. N. 2007, A&A, 466, 413

Reinhardt, C., Chau, A., Stadel, J., et al. 2020, MNRAS, 492, 5336

Safronov, V. S. 1966, Sov.Astron, 9, 987

Sasaki, T., Stewart, G. R. & Ida, S. 2010, ApJ, 714, 1052

Shakura, N. I. & Sunyaev, R. A. 1973, A&A, 500, 33

Slattery, W. L., Benz, W. & Cameron, A. G. W. 1992, Icarus, 99, 167

Tanaka, H., Takeuchi, T., & Ward, W. R. 2002, ApJ, 565, 1257

Tittemore, W. C. & Wisdom, J. 1989, Icarus, 78, 63

Ward, W. R. 1986, Icarus, 67, 164

Ward, W. R. 2017, Journal of Geophysical Research (Planets), 122, 342